Fault Geometry and Slip Distribution at Depth of the 1997 Mw 7.2 Zirkuh Earthquake: Contribution of Near-Field Displacement Data

Mathilde Marchandon, Mathilde Vergnolle, Henriette Sudhaus, Olivier Cavalié

AGU PUBLICATIONS

JGR

Journal of Geophysical Research: Solid Earth

RESEARCH ARTICLE
10.1002/2017JB014703

Key Points:
- Near-field horizontal surface data contribute assessing complexities in fault geometry and slip distribution
- Three main segments broke during the earthquake and acted as asperities separated by geometrical barriers where aftershocks are located
- No shallow slip deficit is found for the overall rupture except on the central segment where it could be due to off-fault deformation in Quaternary deposits

Supporting Information:
- Supporting Information S1

Correspondence to:
M. Marchandon,
marchandon@geoazur.unice.fr

Citation:
Marchandon, M., Vergnolle, M., Sudhaus, H., & Cavalie, O. (2018). Fault geometry and slip distribution at depth of the 1997 Mw 7.2 Zirkuh earthquake: Contribution of near-field displacement data. *Journal of Geophysical Research: Solid Earth*, *123*, 1904–1924. https://doi.org/10.1002/2017JB014703

Received 13 JUL 2017
Accepted 24 JAN 2018
Accepted article online 30 JAN 2018
Published online 15 FEB 2018

Fault Geometry and Slip Distribution at Depth of the 1997 Mw 7.2 Zirkuh Earthquake: Contribution of Near-Field Displacement Data

Mathilde Marchandon[1], Mathilde Vergnolle[1], Henriette Sudhaus[2], and Olivier Cavalié[1]

[1] Université Côte d'Azur, CNRS, Observatoire de la Côte d'Azur, IRD, Géoazur, Valbonne, France, [2] Department of Geosciences, Christian-Albrechts-University Kiel, Kiel, Germany

Abstract In this study, we reestimate the source model of the 1997 Mw 7.2 Zirkuh earthquake (northeastern Iran) by jointly optimizing intermediate-field Interferometry Synthetic Aperture Radar data and near-field optical correlation data using a two-step fault modeling procedure. First, we estimate the geometry of the multisegmented Abiz fault using a genetic algorithm. Then, we discretize the fault segments into subfaults and invert the data to image the slip distribution on the fault. Our joint-data model, although similar to the Interferometry Synthetic Aperture Radar-based model to the first order, highlights differences in the fault dip and slip distribution. Our preferred model is ~80° west dipping in the northern part of the fault, ~75° east dipping in the southern part and shows three disconnected high slip zones separated by low slip zones. The low slip zones are located where the Abiz fault shows geometric complexities and where the aftershocks are located. We interpret this rough slip distribution as three asperities separated by geometrical barriers that impede the rupture propagation. Finally, no shallow slip deficit is found for the overall rupture except on the central segment where it could be due to off-fault deformation in quaternary deposits.

1. Introduction

Measurements of coseismic surface displacements are valuable information to better understand earthquake rupture processes. In the last two decades, the development of space-based geodetic techniques has given access to increasingly complete descriptions of surface displacements induced by earthquakes. In particular, the Interferometry Synthetic Aperture Radar (InSAR) technique has allowed measurement, precisely and over large areas, of the surface displacement field associated with moderate to large crustal earthquakes (Mw > 5), (e.g., Jonsson et al., 2002; Massonnet et al., 1993; Reilinger et al., 2000). Combined with field observations (e.g., fault trace mapping), the high spatial resolution of InSAR data helps to model earthquake characteristics such as fault geometry (e.g., fault dip and segmentation) and fault slip (e.g., Funning et al., 2007; Sudhaus & Jonsson, 2011; Wright et al., 2004). However, when coseismic displacement gradients are too large (typically for gradients greater than 4×10^{-4} when the overall phase correlation is good), the interferometric phase decorrelates near the fault rupture leading to an incomplete description of surface displacements (e.g., Delouis et al., 2002; Hamling et al., 2017; Lasserre et al., 2005; Tong et al., 2010). Moreover, of the three-dimensional surface displacement field, InSAR measures displacements only along one direction, the satellite's line of sight (LOS), which is approximately east-west and downward oriented due to the near-polar orbit of the satellites. Therefore, InSAR measurements from only one LOS do not allow vertical and horizontal motions of the ground to be distinguished. With the combination of ascending and descending LOS measurements, this drawback can be partly overcome, but the sensitivity to any northward displacement is still limited. Consequently, important features of the fault geometry and slip can be missed when modeling the earthquake source using only these data.

The subpixel correlation of optical images can help to improve near-fault data coverage and measurement of all three components of the surface displacement. Since its development for earthquake studies (e.g., Leprince et al., 2007; Michel & Avouac, 2002; Puymbroeck et al., 2000; Rosu et al., 2015), it has been used to measure

coseismic displacement fields of several earthquakes (e.g., Konca et al., 2010; Milliner et al., 2015; Vallage et al., 2015; Wei et al., 2011). By detecting pixel offsets between two optical images that bracket an earthquake, this method gives the north-south (NS) and east-west (EW) coseismic displacement fields with a detection threshold of 1/10 of the image pixel size (Leprince et al., 2007). It has a lower precision than InSAR but it allows measurement of the horizontal displacement field without an upper limit for large surface displacement gradients that usually occur close to the fault. Thus, optical correlation measurements, combined with InSAR data, offer the opportunity to improve the reliability of fault modeling results. Increasing the reliability of fault slip models is crucial because they can constitute the basis of other studies that aim to better understand earthquakes, like analysis of the Coulomb stress changes due to earthquakes (e.g., Hainzl et al., 2009; Parsons, 2004), the comparison between the surface fault slip versus the deep fault slip (e.g., Dolan & Haravitch, 2014), or the estimation of the coseismic stress drop (e.g., Adams et al., 2017). Until now, only a few recent studies combine optical correlation and InSAR data to infer the earthquake source model (e.g., Gombert et al., 2017; Jolivet et al., 2014; Wei et al., 2011).

In this study, we aim to improve our knowledge of the fault rupture geometry and the fault slip of earthquakes, by investigating joint optimization of intermediate-field InSAR and near-field optical data. We focus on the 1997 Mw 7.2 Zirkuh, Iran earthquake, that exhibits a complex fault geometry and rupture pattern according to field measurements, seismological data, and an InSAR-based fault source model (Berberian et al., 1999; Sudhaus & Jonsson, 2011) and for which previous studies lack high-resolution horizontal and near-field surface measurements. We complement the InSAR data set of Sudhaus and Jonsson (2011) with the horizontal displacement field of the earthquake measured by subpixel correlation of satellite optical images to refine the fault model for the earthquake. This presents two challenges. First, we have to deal with two types of high spatial resolution data, which implies that the error estimation and the data weighting of each type of data set must be done rigorously. Second, optimizing both the fault geometry and the slip distribution involves many parameters so we use a two-step fault modeling procedure. We discretize the fault into several segments along the strike and use a genetic algorithm (Sambridge & Mosegaard, 2002; Smith et al., 1992) to estimate the dip and slip of each fault segment. Once the fault geometry is determined, we divide each fault segment into subfaults to image in more detail the slip distribution at depth.

2. The 1997 Mw 7.2 Zirkuh Earthquake

The Mw 7.2 Zirkuh earthquake broke the entire NNW-SSE Abiz right-lateral strike-slip fault in northeast Lut (northeastern Iran, Figure 1) on 10 May 1997, as the last event of an 11-earthquake seismic sequence in this area (Berberian & Yeats, 1999). Field investigations made after the Zirkuh earthquake by Berberian et al. (1999) showed a complex surface trace due to a multisegmented rupture, where the shear at the fault was narrowly localized in some places and more broadly distributed in others. Horizontal right-lateral fault offsets varied strongly, ranging typically between 80 cm and 140 cm with a maximum of 230 cm in the southern part of the rupture. Moreover, some parts of the fault displayed significant reverse faulting (up to 90 cm in the south).

The complexity of the Zirkuh earthquake is also highlighted by the analysis of body wave seismograms that suggest the Zirkuh earthquake happened in four subevents, with significant changes of the orientation of faulting (Berberian et al., 1999). The rupture started in the north with a pure right-lateral strike-slip mechanism, propagated southward with an oblique mechanism on a fault dipping to the west, continued with a strike-slip subevent, and finally ended in the south with a pure reverse mechanism on an east dipping fault (Figure 1b).

The seismologically inferred changes in faulting orientation are supported by the geodetic study of Sudhaus and Jonsson (2011). They inferred the first multisegmented fault slip model of the earthquake based on four SAR interferograms. Their estimated fault geometry is west dipping in the northern part of the fault, nearly vertical in the central part and east dipping at the southern end. Their results are consistent with Berberian et al. (1999) to the first order.

3. Data

3.1. InSAR Data

The four interferograms of the Zirkuh earthquake used in this study have been processed by Sudhaus and Jonsson (2011). This InSAR data set is composed of two descending ERS-2 interferograms (IG1 and IG4, Figures 1c and 1e), one ascending ERS-1/2 interferogram (IG3, Figure 1d) and one descending JERS-1 interferogram

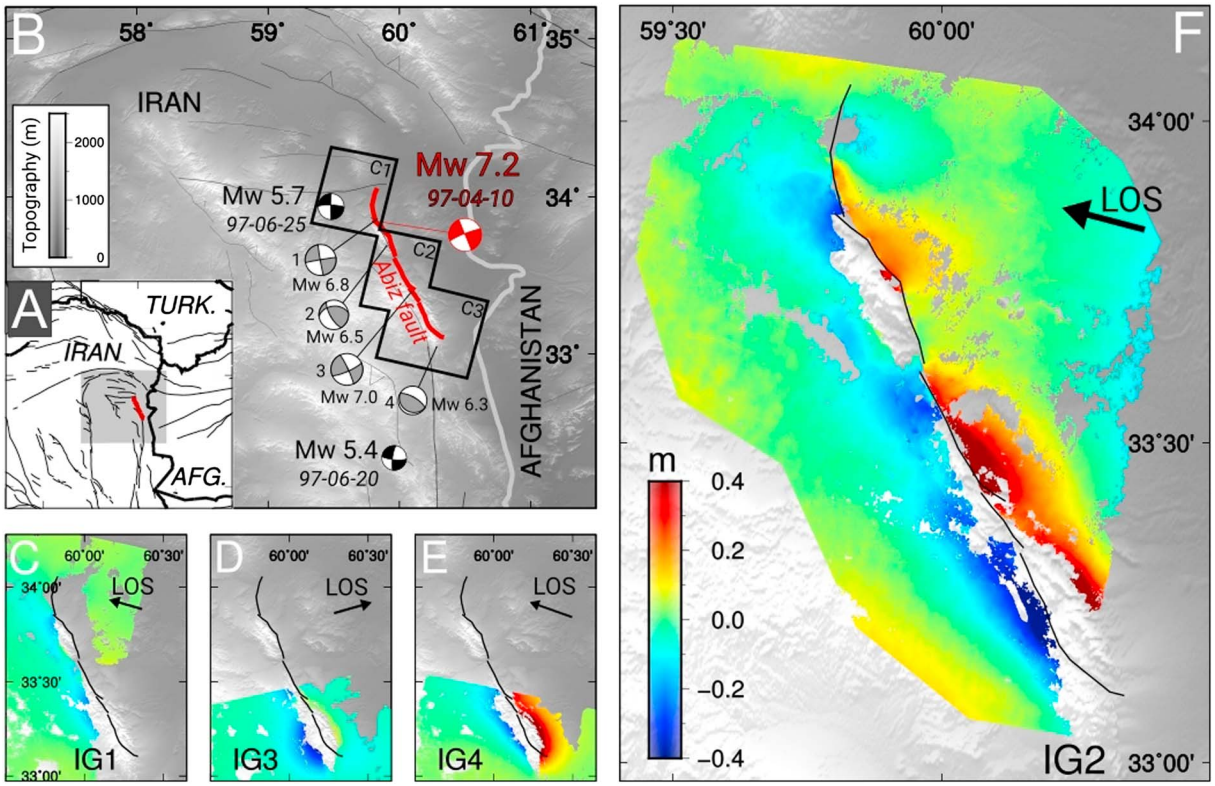

Figure 1. Regional tectonic overview and InSAR data. (a) Map of eastern Iran, bordering Turkmenistan (TURK) and Afghanistan (AFG) showing the main tectonic faults (thin black lines), the Abiz fault (red thick line), and the coverage of the study area in Figure 1b (gray box). (b) Topographic map of the study area showing major faults of the region (thin black lines) with the surface trace of the Zirkuh earthquake (thick red line) and the coverage of optical correlation data (black boxes C1, C2, and C3 and Table 2). Moment tensor solutions of the main shock and the two largest aftershocks are represented in red and black beachballs, respectively (after Berberian et al., 1999; Engdahl et al., 2006). The moment tensors of four subevents inferred by the seismological study of Berberian et al. (1999) are represented in gray. (c–f) Unwrapped interferograms from ERS1/2 and JERS-1 SAR images processed by Sudhaus and Jonsson (2011) (Table 1). The arrows indicate the LOS (line of sight) direction. Positive displacement indicates a movement of the ground toward the satellite.

(IG2, Figure 1f). The interferogram characteristics are listed in Table 1. IG1 and IG2 cover nearly the entire rupture, whereas IG3 and IG4 cover only the southern half. All interferograms display phase decorrelation near the fault trace. Only IG2, which is an L-band interferogram, succeeds in measuring the displacements up to the fault trace along some parts of the rupture. Hence, this data set mostly does not provide measurements closer than ~10 km to the surface trace of the fault but precisely measure the intermediate displacement field (here farther than 10 km from the fault, Figures 1c–f). Moreover, due to the NNW-SSE orientation of the Abiz fault, the satellite LOS, which is nearly perpendicular to the fault strike, is poorly sensitive to the main component of this mostly purely strike-slip event.

3.2. Optical Correlation Data

To measure the horizontal displacement field of the Zirkuh earthquake, we use pre-earthquake and post-earthquake Satellite Pour l'Observation de la Terre (SPOT) satellite images. Three image pairs are needed to cover the entire surface rupture (Figure 1b and Table 2).

Table 1
Sensor, Acquisition Time, and Geometry Information of the SAR Interferograms

IG[a]	Sensor	Wavelength (cm)	Pass	Track	Frame	Master date	Slave date	Bperp[b]	Time span (years)
IG1	ERS-2	5.6 (C-band)	desc.	120	2925; 2943	96/04/03	99/03/24	136	2.97
IG2	JERS-1	23.5 (L-band)	desc.	209	244; 245	94/11/15	97/07/10	1,060	3.07
IG3	ERS-1/2	5.6 (C-band)	asc.	70	657	96/03/30	98/08/22	21	2.39
IG4	ERS-2	5.6 (C-band)	desc.	349	2943	96/05/24	98/09/11	25	2.30

[a]Interferogram. [b]Perpendicular baseline in meters.

Table 2
SPOT Optical Satellite Image Metadata

Displacement map	Sensor	Resolution (m)	Date (year-month-day)	Time Span (years)	Incidence angle (deg)
C1	SPOT 2	10	91-08-27	14.3	−0.5
	SPOT 2	10	05-09-04		−1
C2	SPOT 2	10	91-08-22	8.8	2.3
	SPOT 4	10	00-06-02		2.9
C3	SPOT 3	10	95-10-05	6.42	25.8
	SPOT 4	10	02-03-08		26.1

Note. SPOT = Satellite Pour l'Observation de la Terre.

We follow the methodology described in Ayoub et al. (2015) using the Coregistration of Optically Sensed Images and Correlation (COSI-Corr) software package (Leprince et al., 2007). First, the post-earthquake image is orthorectified using the information in its ancillary file (position, attitude, and look direction of the satellite), the 30 m ASTER Global Digital Elevation Model (DEM) and a shaded version of this DEM. Then, the pre-earthquake image is orthorectified and coregistered to the post-earthquake orthoimage using four tie points located far away from the deformation zone. The pre- and post-earthquake orthoimages are correlated using a multiscale sliding correlation window of 128 to 64 pixels with a step size of 8 pixels (80 m). Measurements with a low signal-to-noise ratio (<0.90) and outliers with displacement values higher than ±5 m are masked out. We consider surface displacements larger than 5 m unrealistic as the maximum field-measured offset is 2.30 m. Along-track undulations due to CCD (Charge-Coupled Device) array artifacts are removed by stacking and subtracting the average artifact signal from the correlation (Leprince et al., 2007). Finally, high-frequency noise is reduced using the nonlocal mean filter (Buades et al., 2008) implemented in COSI-Corr with a noise parameter value of ~0.4, a patch size of 5 by 5 pixels and a search area dimension of 21 by 21 pixels (Ayoub et al., 2015).

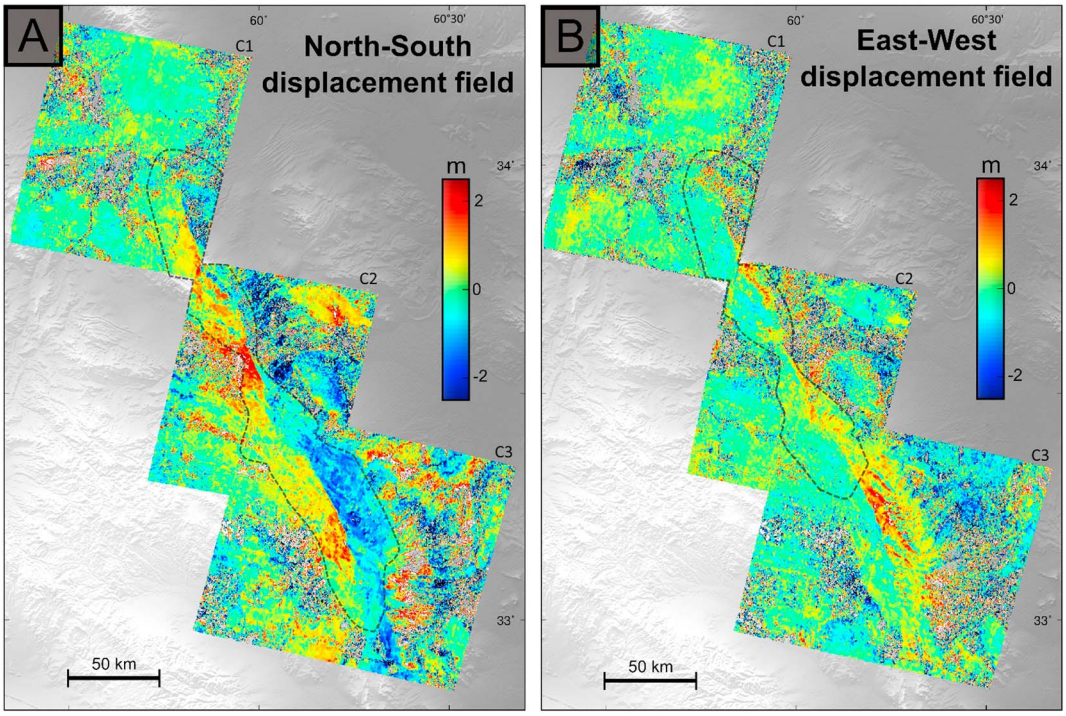

Figure 2. North-south (a) and east-west (b) displacement field (m) for the Zirkuh earthquake measured from correlation of pre-earthquake and post-earthquake SPOT optical images. Displacements are positive northward in (a) and eastward in (b). The dashed gray lines delimit the area of data used in the optimization.

Figure 2 displays the NS and EW measured surface displacements of the Zirkuh earthquake. The NNW-SSE surface trace of the rupture is clearly visible in the NS displacement field and shows many variations of fault strike along the trace (Figure 2a). In the C1, C3 displacement maps (Figure 1b and Table 2) and in the central part of the C2 displacement map (Figure 2a), the deformation is localized across the fault (i.e., discontinuity step in the surface displacement field) and the surface displacements exceed 2 m. These three zones of localized deformation are separated by zones of distributed deformation, which are zones where the surface displacements change gradually across the fault. In these zones, the surface trace of the fault is not easily discernible and displacements are smaller than 1 m. Finally, the displacement field is not symmetric across the fault. Indeed, in the central part of the rupture, the maximum displacement is found in the western part of the fault (C2 displacement map), whereas in the south it is maximal on the eastern side of the fault (C3 displacement map).

Due to the strike-slip mechanism and NNW-SSE orientation of the Abiz fault, the EW displacements are smaller than the NS displacements and in general do not exceed 1 m (Figure 2b). The fault trace is thus much harder to discern than on the NS displacement field. Nevertheless, we can still detect the zones where deformation is either localized or distributed. The EW displacements displayed in the southern part (C3 displacement map) and eastern side of the fault show a topography-correlated signal. This signal is due to the topography that was locally changed by the earthquake and off-nadir image look angles (Table 2), while using only one DEM (here, post-earthquake DEM) to orthorectify both pre- and post-earthquake images (Ayoub et al., 2009). This problem affects mostly the EW displacement component because the SPOT satellite orbit is nearly NS and the viewing angle of the SPOT satellite can only be adjusted in the across-track direction. Correction of this artifact is only possible when vertical displacements are negligible (Ayoub et al., 2009), which is not the case in the southern part of the rupture (Berberian et al., 1999; Sudhaus & Jonsson, 2011). Indeed, part of the vertical displacement is projected into the apparent EW displacement. For this reason, we exclude the EW displacement field measured with the C3 image pair (Table 2) in the modeling.

Finally, some parts of the displacement field are dominated by nontectonic signal or decorrelation due to the long time span that separates the pre- and post-earthquake images (about 9 years, see Table 2). We exclude these areas and use only the data close to the fault that are dominated by the coseismic signal (Figure 2) in the optimization. The remaining area of useful optical data covers the data gap in the InSAR data caused by phase decorrelation. In the following sections, all the data are projected onto Cartesian UTM coordinates (UTM zone 40S).

3.3. Error Estimation and Data Subsampling

InSAR data, as well as optical-correlation displacement data, contain both spatially correlated and uncorrelated nontectonic signals. To weight the data in the optimization proportionally to their precision, these error characteristics have to be taken into account. For InSAR measurements, the spatially correlated signal is mostly due to phase propagation delays through the atmosphere, while the uncorrelated noise is caused by phase decorrelation or small-area unwrapping errors (Hanssen, 2001). For the optical correlation technique, spatially correlated noise can come from topography unaccounted for by the DEM (e.g., if the DEM has a much coarser spatial resolution than the image resolution) or when the difference in sun shading between the pre- and post-earthquake images is very large. The processes that change the Earth's surface between the acquisition of the pre- and post-earthquake optical images (deposition of sediment, erosion, or anthropogenic sources) can result in both uncorrelated and spatially correlated errors. Here we describe these different sources of noise with a geostatistical approach by estimating empirically covariograms and semivariograms for each data set.

For the InSAR data set, we follow the methodology presented in Sudhaus and Jonsson (2009) and calculate empirical semivariograms and covariograms in the nondeformed parts of the interferograms. The covariograms describe the correlated data error of the data set, whereas from the semivariograms we can estimate the uncorrelated (white) noise. The underlying assumption is that the noise is Gaussian around a mean value of zero and stationary. The latter assumptions imply that the noise structure estimated in nondeformed areas is representative of the entire interferogram.

For optical data, the noise structure cannot be considered stationary because the sources of noise in nondeformed areas are not representative of the entire displacement map (see Figure 2). Therefore, we estimate the noise structure in the near-field of the fault. However, in this area, the signal is dominated by the coseismic displacements. We thus use an approach similar to Jolivet et al. (2014). We first estimate the tectonic

signal by inverting the data of each displacement map using a least squares fault slip inversion and making the assumption of an elastic homogeneous half-space (Okada, 1992). Then, we subtract the synthetic data of the best fit fault slip model from the observations. Finally, we estimate the semivariograms and covariograms on these data residuals. The noise analysis of the data residuals shows short-period signals and noise. The short-periodic content is partly a result of the correlation processing method itself, the step size being smaller than the sliding window size (section 3.2). The data are therefore correlated on length scales of up to the largest window size used, which is 128 pixels and has a corresponding extent of 1.3 km. The short-periodic content is also a result of other contributions, which we assume to be nontectonic. These correlations are taken into account in the estimation of the noise structure of optical displacement maps (see the example of the C3 displacement map in the supporting information Figure S1a). This method may exclude and underestimate data errors with longer spatial periods.

The empirical covariograms and semivariograms are estimated by calculating the covariance (equation (1)) and variance (equation (2)) of pixel pairs separated by a certain distance range centered at h_c and that we randomly sample on each residual of the five optical data sets:

$$C(h_c) = \frac{1}{2N} \sum_{\substack{i=1 \\ ||r_i - s_i|| \approx h_c}}^{N} d(r_i) \cdot d(s_i), \tag{1}$$

$$V(h_c) = \frac{1}{2N} \sum_{\substack{i=1 \\ ||r_i - s_i|| \approx h_c}}^{N} [d(r_i) - d(s_i)]^2. \tag{2}$$

where N is the number of data pairs, and $d(r_i)$ and $d(s_i)$ are the data values at locations r_i and s_i such that $|r_i - s_i| \approx h_c$. We compute the empirical covariograms and semivariograms, $C(h_c)$ and $V(h_c)$, respectively, for distances ranging from 0.5 km to 30 km (Figures S1b and S1c in the supporting information). On the empirical covariograms, we then fit positive-definite covariance functions (Figure S1b and Table S1 in the supporting information) of the form:

$$\mathrm{Cov}(h) = b \exp\left(\frac{-h}{a}\right). \tag{3}$$

where h is the distance (km) and a and b are the coefficients to determine. The data error variance is estimated from the plateau of the empirical semivariogram (Figure S1c and Table S1 in the supporting information, Chilés & Delfiner, 1999). The covariance function and variance are unique for one data set: the noise level variations within one data set cannot be estimated but the noise level between each data set can be compared.

The covariance functions and variances for the five optical data sets and the four interferograms are represented in Figures 3a and 3b, respectively. The correlation length is less than 1 km in the C1 and C2 displacements and less than 2 km in the C3 displacements, which means that the noise is more spatially correlated in C3 than in C1 and C2 (Figure 3). The correlation lengths are approximately equal to the largest window size of 1.3 km used in the processing of the optical images. It confirms that the data processing technique impacts the data covariance. The variance is higher for C1 (0.8 m^2 and 0.6 m^2 for C1 EW and C1 NS, respectively) than for C2 (0.2 m^2) and C3 correlation (0.3 m^2, Figure 3). These values are a good example of uncorrelated noise observed in the data due to the temporal decorrelation. Indeed, C1 shows an important part of incoherent noise on the eastern part of the fault, this noise being limited for C2 and C3 (Figure 2). In the InSAR data, the noise level is lower but the correlation length is larger (up to 20 km). This length scale is characteristic of the turbulent atmospheric pattern that produces spatially heterogeneous phase delays in the interferograms. The covariances and variances are about 3 orders of magnitude smaller than those for optical-correlation displacement data (Figure 3 and Table S1). This quantifies the higher precision of the InSAR data compared to the optical data, as is visually apparent in this case study. In the following, the covariance functions and variances will be used to build the weighting matrix (see section 4.2.2).

In order to limit the computation time for optimization and because of memory limitation, we reduce the number of data points using a quadtree algorithm (Jonsson et al., 2002). The quadtree algorithm keeps high spatial sampling in areas where the displacement gradient is high, while it down-samples data in areas where the displacement gradient is low. It thus allows us to reduce the number of data points from more than 12 million to 7877, without loss of relevant information. Averaging during the down-sampling process also increases the signal-to-noise ratio.

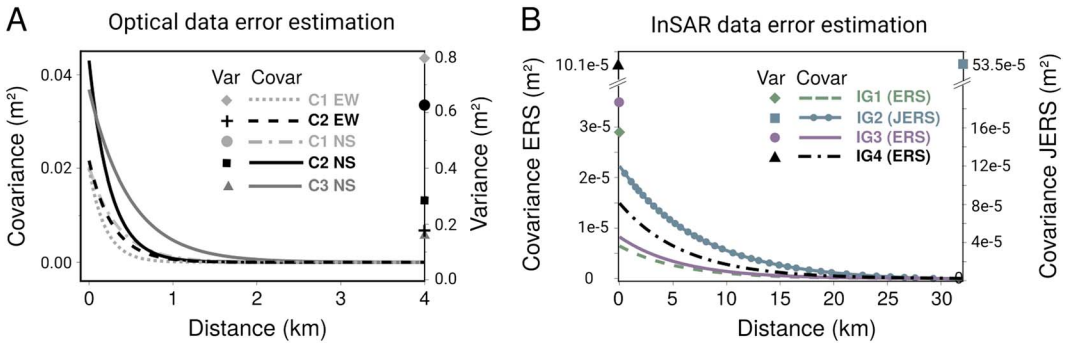

Figure 3. Estimated variances and covariances of data noise for the (a) optical data and (b) InSAR data. Note that due to large differences in the error values, left and right *y* axes show different scales.

4. Two-Step Fault Modeling

4.1. Parametrization of the Fault and Optimization Strategy

The surface trace of the rupture, mapped from both field measurements and optical-correlation displacement data, shows that the Abiz fault has a complex structure. It is curved in its northern part and has many fault strike variations on its southern continuation (see Figure 2 and Berberian et al., 1999). We thus model the fault with 16 segments according to the surface trace mapped with optical-correlation displacement data (Figure 4).

The seismological study of Berberian et al. (1999) shows that the mechanism of faulting during the Zirkuh earthquake changes from north to south. While being predominantly a right-lateral strike-slip earthquake, it includes considerable thrust components. We therefore have to expect changes in the fault dip along the Abiz fault, but little information is available concerning this fault parameter. It is thus essential to estimate the geometry of each segment before inverting the spatial distribution of slip on the fault. We therefore choose a two-step optimization strategy. First, we estimate the geometry and a uniform slip value for each segment using a genetic optimization algorithm (Sambridge & Mosegaard, 2002; Smith et al., 1992). This algorithm allows us to sample a large model parameter space in order to find the model that minimizes the misfit *e* (equation (4)) between the data $\mathbf{d}_{obs}$ and the model predictions $\mathbf{d}_{pred}$:

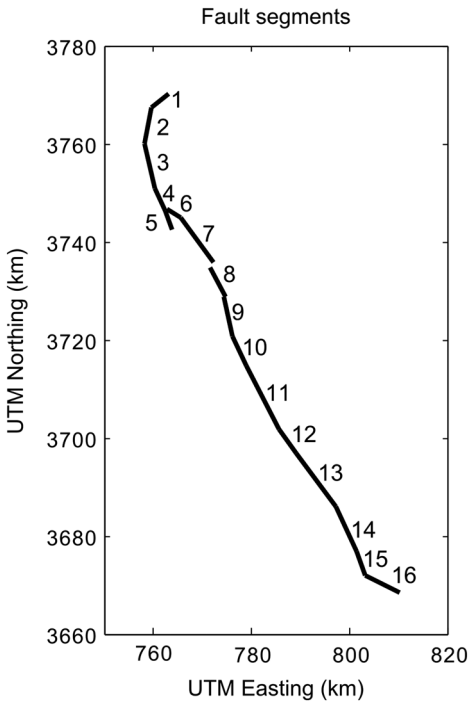

Figure 4. Outline of the Abiz fault model with 16 segments that precisely follow the surface trace mapped using the optical-correlation displacement maps (Figure 2).

$$e = \sqrt{(\mathbf{R}(\mathbf{d}_{obs} - \mathbf{d}_{pred}))^{T} \quad \mathbf{R}(\mathbf{d}_{obs} - \mathbf{d}_{pred})}, \tag{4}$$

$$e_{tot} = e + e_{dip}. \tag{5}$$

The data residuals ($\mathbf{d}_{obs} - \mathbf{d}_{pred}$) are weighted by the matrix **R** depending on the data error (see sections 3.3 and 4.2.2) and the redundancy of the data (see section 4.2.2). We also add to the misfit *e* a penalty function e_{dip} to constrain the algorithm to sample models with limited dip angle fluctuations between neighboring segments (see equation (5) and section 4.2.3).

Second, we fix the geometry of the optimum fault model and discretize the fault segments in subfaults to invert for a more detailed slip distribution. In both steps, the rupture is modeled as a dislocation embedded in an elastic half-space (Okada, 1992) with a Poisson's ratio of 0.25.

4.2. Step 1: Nonlinear Fault Segment Optimization Using a Genetic Algorithm

4.2.1. Model Parametrization and Model Space Exploration

The genetic algorithm is a global optimization method inspired by natural selection (Beyer & Schwefel, 2002; Monelli & Mai, 2008; Sambridge & Mosegaard, 2002; Smith et al., 1992). In such optimizations, models are considered as the individuals of a population that improve their characteristics (parameters) through the processes of recombination, mutation, and selection over several generations. The genetic algorithm allows for

Table 3
Predefined Bounds for the Fault Model Parameters

	Width (km)	Dip	Strike-slip (m)	Dip-slip (m)
Lower bound	0	60°W	0	−1.5
Upper bound	15	60°E	5	1.5

an efficient exploration of the model space and permits finding optimum models that are close to the global minimum of the misfit function e_{tot} (equation (5)).

The exploration of the model parameter space starts by picking randomly a certain number of models called the parent generation. In our case, one fault model is described by 64 parameters: the segment width, dip angle, and strike-slip and dip-slip components of the 16 segments. The values of the model parameters are chosen within individual predefined bounds (Table 3). Then the parameters of the parent fault models are recombined to a larger number of models and mutated to form the offspring fault models. The mutation process consists of slightly changing the model parameter values of the fault models. A standard deviation, defined as a percentage of the corresponding model parameter range, controls that change. Finally, the misfit e_{tot} (equation (5)) is calculated and a certain number of the low-misfit offspring fault models are kept to form the next parent model generation. This loop is repeated for several generations as the misfit continues to decrease significantly.

The number of parent models and offspring models, as well as the parameter preset bounds and standard deviation, which governs the intensity of the mutation, fully control how the parameter space is explored. We choose to divide the optimization process in four stages. The characteristics of each stage and the misfit through the four stages can be found in Figure 5a, while Figure 5b illustrates the model space exploration for the parameters of one representative fault segment. The first stage allows exploring of the entire model space (Figure 5b) and to eliminate zones with high misfit thanks to the large standard deviation of 5%. In stages 2 and 3, to focus the search to low misfit zones, we decrease the parameter standard deviations to 2% and 1%, respectively, but increase the parent and offspring numbers to sample these low misfit zones intensively. Finally, we increase the number of generations from 15 during stages 1, 2, and 3 to 70 during stage 4, to carefully sample the parameter space around the global minimum misfit. Through this process, the misfit decreases (Figure 5a) and the search converges into a shrinking model space as shown by the location of the 200 best models of stage 4 (Figure 5b). Finally, the misfit no longer decreases significantly and the best model is picked based on the misfit criteria.

While Figure 5b shows a good convergence for the fault dip, strike-slip, and dip-slip parameters during the optimization, it shows a poor convergence for the fault width. This information is also illustrated by frequency histograms in Figure 5c. They show clear single peaks for all model parameters except the fault width for which the frequency is quite homogeneously distributed, for example, between 8 and 11 km for segment 11. This pattern repeats for all segments, which means that the data cannot well constrain the width. We thus choose to fix the width and to optimize only the dip, strike-slip, and dip-slip (Tables S2 and S3 in the supporting information). We also enlarge the bandwidth for the search when the initial bounds for one parameter are too restrictive and we fix a few other parameters that do not seem well constrained (see Tables S2 and S3) to stabilize the optimization. Together with the 48 parameters of the Abiz fault (16 segments × 3 parameters), we search for residual orbital ramps in the InSAR data as a linear function. Finally, we optimize the slip of the two main aftershocks that could affect the surface displacement data, which adds four more model parameters. We thus optimize a total number of 66 model parameters. A single four-stage optimization with 95200 forward model calculations takes 15 h on an eight-processor workstation.

In order to identify the impact of optical data on the model result, we run two optimizations: one using only InSAR data (InSAR-based model) and the second using InSAR and optical data jointly (joint-data model). The constraints of the InSAR-based and the joint-data models are summed up in Tables S2 and S3 in the supporting information. The parameter bound investigation for the InSAR-based model gives results similar to the evaluation done by Sudhaus and Jonsson (2011). Thus, we keep the same constraints that allow us to derive

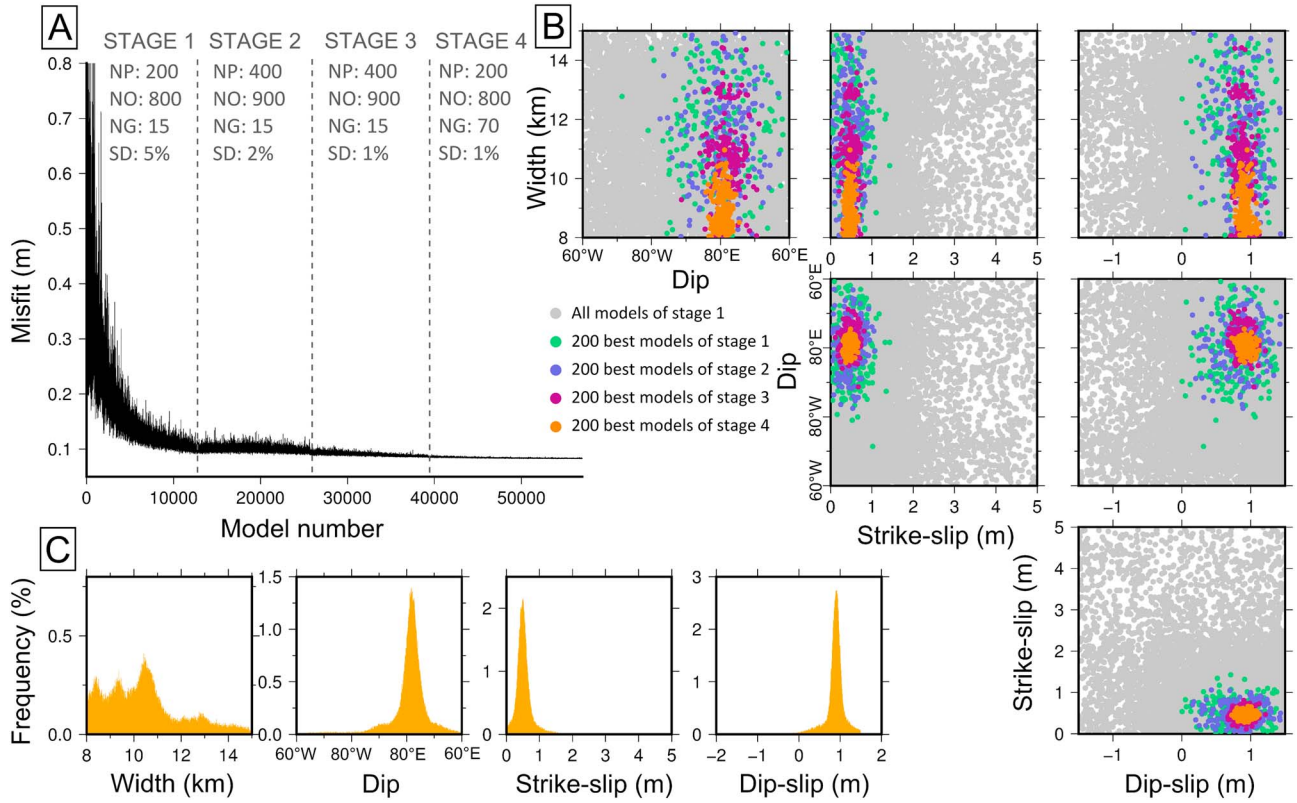

Figure 5. Misfit and space exploration by the genetic algorithm. (a) Misfit (m) as a function of model number. Abbreviated terms are number of parents (NP), number of offspring (NO), number of generations (NG), and standard deviation (SD). (b) Exploration of the model space through the four stages of the optimization (example of segment 11 (joint-data optimization), Figure 4). The points represent the models visited during the four stages. The gray points show all models of stage 1 and colored points show the 200 best models of stages 1 (green), 2 (blue), 3 (fuchsia), and 4 (orange). (c) Histograms representing the frequency of the parameter values visited during the optimization (all stages, segment 11).

an almost equivalent model as Sudhaus and Jonsson (2011), despite small changes in the discretization of the Abiz fault.

4.2.2. Data Weighting

Data are weighted by the matrix **R** (equation (4)) that takes into account the noise structure and the redundancy of the data. We use the covariance functions and the variance of the noise (section 3.3) to define the full-resolution variance-covariance matrix $\mathbf{\Sigma}_f$. The diagonal elements of the matrix contain the variance of each data point, whereas the off-diagonal elements contain the covariance of each possible point pair. The data being subsampled, we form the subsampled variance-covariance matrix $\mathbf{\Sigma}$ with

$$\mathbf{\Sigma} = \mathbf{A}\mathbf{\Sigma}_f\mathbf{A}^T. \tag{6}$$

where **A** is the operator relating the full data vector $\mathbf{d}_f$ to the subsampled data vector **d**:

$$\mathbf{d} = \mathbf{A}\mathbf{d}_f. \tag{7}$$

Then, we compute the weighting matrix **R** based on the subsampled variance-covariance matrix $\mathbf{\Sigma}$ with

$$\mathbf{\Sigma}^{-1} = \mathbf{R}^T\mathbf{R}. \tag{8}$$

The final data weight depends on the variance and covariance of the data set. High variance corresponds to low weight and high correlation corresponds to low weight. Furthermore, a higher number of pixels in a quadtree square increases the weight.

With the InSAR variances and covariances being 3 orders of magnitude smaller than those of optical data (Figure 3 and section 3.3), InSAR data prevail over optical data in the optimization. As a consequence, optical data are not well reproduced at the end of the optimization. We thus introduce an ad hoc factor, based on a balanced fit to the InSAR and optical data, to adjust the two data set weights. We find an optical data weight over InSAR data weight ratio of 0.3 (Figure S2 in the supporting information). By doing this, we no longer take

into account the absolute error of optical data with respect to the absolute error of InSAR data, but we still keep the relative errors within each data set type (InSAR or optical data).

We use nine data sets with different footprints to cover the entire Zirkuh rupture. As a consequence, not all observation points of the field are covered by the same number of data (Figure S3a in the supporting information). Some areas are covered by four overlapping data sets (mainly in the intermediate field), some by three (mainly in the near-field), and up to seven for areas mapped with both types of data. In the current weighting matrix **R**, the points with multiple observations have artificially higher weights in the optimization, which is justified only if the observations are independent. However, observations are entirely independent only if they have perpendicular look vectors (e.g., NS and EW components for the optical correlation) and linearly dependent otherwise. We thus calculate an overlay ratio that reflects the linear dependency between different observations at a single location (Sudhaus & Jonsson, 2011). For each location, we list the look vector of the M overlapping data sets in the matrix $\mathbf{L}_v$. We compute the matrix **V** that gives the scalar product between each look vector of the M overlapping data sets ($\mathbf{V} = \mathbf{L}_v \cdot \mathbf{L}_v^T$). The sum of each line of the matrix **V** ($\mathbf{v} = \sum_{j=1}^{M} |\mathbf{V}_{ij}|$) gives information about the linear dependency between each data set that we use to calculate the overlay ratio of each observation ($w_i = \frac{1}{\sqrt{v_i}}$). The overlay ratio w_i is equal to 1 if the observation is independent from the other data sets and less than 1 otherwise (Figure S3b in the supporting information). Finally, the vector of overlay ratio **w**, composed of the overlay ratio of each data point w_i, is taken into account in the weighing by multiplying the error matrix **R** by **w**.

4.2.3. Dip Smoothing

For some segments, we note that the dip parameter is hard to constrain. We thus use a penalty function e_{dip} to limit dip fluctuations between neighboring segments. Following Sudhaus and Jonsson (2011), we express e_{dip} as

$$e_{\text{dip}} = \kappa_{\text{dip}} \sum_{k=1}^{N-1} \frac{x_{\text{dip},k} - x_{\text{dip},k+1}}{((l_k - l_{k+1})/2)^2}, \tag{9}$$

where N is the number of segments, $x_{\text{dip},k}$ and l_k are the dip and length of the kth segment, respectively, and κ_{dip} is the smoothing factor that controls the dip smoothing intensity. According to equation (9), e_{dip} is large when adjacent segments have big differences in dip. The penalty function is added to the misfit e (equation (4)) to form the total misfit e_{tot} (equation (5)). Consequently, in the genetic algorithm, sampled models with large variations of dip will be rejected during the process of model selection, except if the dip variation is strongly required by the data. The preferred smoothing factor, chosen subjectively after running several tests, limits the dip fluctuations between neighboring segments without deteriorating the fit of the model predictions to the data.

4.3. Step 2: A Constrained Least Squares Distributed Slip Inversion

4.3.1. Method

Once the geometry is fixed, we divide the fault segments into subfaults and invert the data to retrieve the slip distribution on the fault using a constrained linear least squares inversion using the algorithm of Coleman and Li (1992). The strike-slip and dip-slip are constrained to values between 0 m and 10 m and −10 m and 10 m, respectively, to avoid models with unreasonable slip patterns. We also implement a Laplacian smoothing operator to reduce the slip variations between neighboring patches (Jonsson et al., 2002). We thus resolve the following system of equation:

$$\begin{bmatrix} \mathbf{d}' \\ 0 \end{bmatrix} = \begin{bmatrix} \mathbf{G}' \\ \lambda \mathbf{D} \end{bmatrix} \mathbf{m}. \tag{10}$$

where $\mathbf{d}'$ is the weighted data vector ($\mathbf{d}' = \mathbf{Rd}$), $\mathbf{G}'$ the weighted Green's function matrix relating the surface displacements to the slip model ($\mathbf{G}' = \mathbf{RG}$), **m** the vector of parameters we are solving for (i.e., strike-slip and dip-slip on each subfault), **D** the second-order finite difference operator and λ the smoothing factor. We set λ according to an L-curve criterion (see Figure S4 in the supporting information).

In the optical correlation displacement field, pixels at the rupture trace can result in zero displacements due to the correlation window that crosses the fault. In the optimization procedure, this artifact does not impact the model results as the slip is uniform from surface to depth on each segment. However, it can induce very low slip at shallow depths in the distributed slip inversion. Therefore, we remove the two pixels (i.e., 2 km) surrounding the fault but we additionally invert for offsets localized across the fault to keep the near-field coverage (Xu et al., 2016). These offsets are measured from profiles of 10 km length across strike and stacked

over a 2 km width along strike. The offsets are weighted in the inversion by the square root of the inverse of the mean standard deviation of the stacked profile.

4.3.2. Fault Plane Discretization

Fault planes are usually discretized into subfaults of constant size. However, it is well known that surface data hardly constrain slip on the deepest subfaults. Indeed, the amplitude of static displacements decreases with the inverse square of the distance to the fault (Page et al., 2009). Therefore, deep slip has much less influence on the surface data than shallow slip (Atzori et al., 2012; Barnhart & Lohman, 2010). We compute the data sensitivity to subfault slip to quantify the weight of each subfault on the surface data. The parameter is defined as the sum of surface displacement induced by a unit slip on the considered patch divided by the number of data (equation (11)):

$$S_k = \frac{\sum_{i=1}^{N} u_{s,i} + \sum_{i=1}^{N} u_{d,i}}{N}. \tag{11}$$

where S_k is the sensitivity of the kth subfault, $u_{s,i}$ and $u_{d,i}$ are the surface displacement for the data point i due to 1 m of strike-slip and dip-slip, respectively, on subfault k, and N the number of surface data. For a homogeneous discretization (Figure S5a in supporting information), the subfaults located below a depth of 5 km have very little influence on the surface data (sensitivity of less than 0.005 m). We thus choose to manually discretize the fault plane into variable size subfaults in order to homogenize the sensitivity on the fault (Figure S5b in supporting information). The fault is discretized into 252 subfaults of about 2 km by 2 km at the surface and 5 km by 5 km at greater depths. With the increase of subfault size with depth, the sensitivity on the fault ranges from 0.007 m to 0.03 m whereas it ranges from 2.5×10^{-5} m to 0.03 m with a homogeneous discretization.

5. Results

5.1. Uniform-Slip Segment Model Results

Figure 6 shows the optical data and predictions of the uniform InSAR-based and joint-data models. Both models reproduce the first-order pattern of the optical surface displacement well and have a good global root mean square (RMS) misfit between optical data and predictions with respect to the data precision (Figure 6). However, the models do not reproduce the second-order pattern equally. In particular, the InSAR-based model does not reproduce the high NS surface displacements located in the center part (near 3,720 km northing) and in the southern part (from 3,670 km to 3,690 km northing) of the fault and overestimates the NS displacements in the north (near 3,750 km northing). On the contrary, the joint-data model succeeds in predicting the three zones of higher displacements, which are main features of the NS optical data. Regarding the EW optical data, which have a lower signal-to-noise ratio than the NS optical data due to the fault orientation, predictions from both models are similar. As expected, the joint-data model is less effective at predicting the InSAR displacements than the InSAR-based model (Figure 7). However, both models reproduce the main surface displacement features displayed by InSAR data and no significant difference is observed. As a consequence, the RMS misfit between optical data and predictions is 15% lower in the joint-data model than in the InSAR-based model, whereas the RMS misfit between InSAR data and predictions only slightly deteriorates in the joint-data model (see RMS misfit in Figure 7).

Figure 8 shows a top view and a side view of the fault geometry and slip distribution of the best fit models. The InSAR-based fault optimization results are consistent with those published by Sudhaus and Jonsson (2011) (Figure 8). The northern part of the fault (segments 1–6) is dipping 80°W, while the southern part of the fault is dipping 85°E (segments 7–16). The slip distribution along the different segments is homogeneous with about 1.2 m from segment 7 to 13 and has two maxima of 2.3 m in the north (segments 3–4) and 2 m in the south (segments 14–15). The slip is almost purely strike-slip all along the fault and shows a significant reverse component only on the southernmost two segments where the rake turns to about 146°.

The joint-data optimization shows several important differences in the fault plane geometry and slip distribution. First, for the joint-data model, the fault dips are much less vertical than those found for the InSAR-based model. The northern part of the fault dips westward on a more extended portion from segment 1 to 10 at an angle of about 79° W. In the southern part (segments 11–16), the fault dip is also eastward but with an angle of 75°E. Second, the slip distribution along the fault is also noticeably different, with three zones of high slip: 2 m on segments 4 to 5 in the north, 2.1 m on segment 10 in the center, and 2.8 m on segments 13 to 15 in the south. These zones of high slip are separated by segments on which slip does not exceed 1 m.

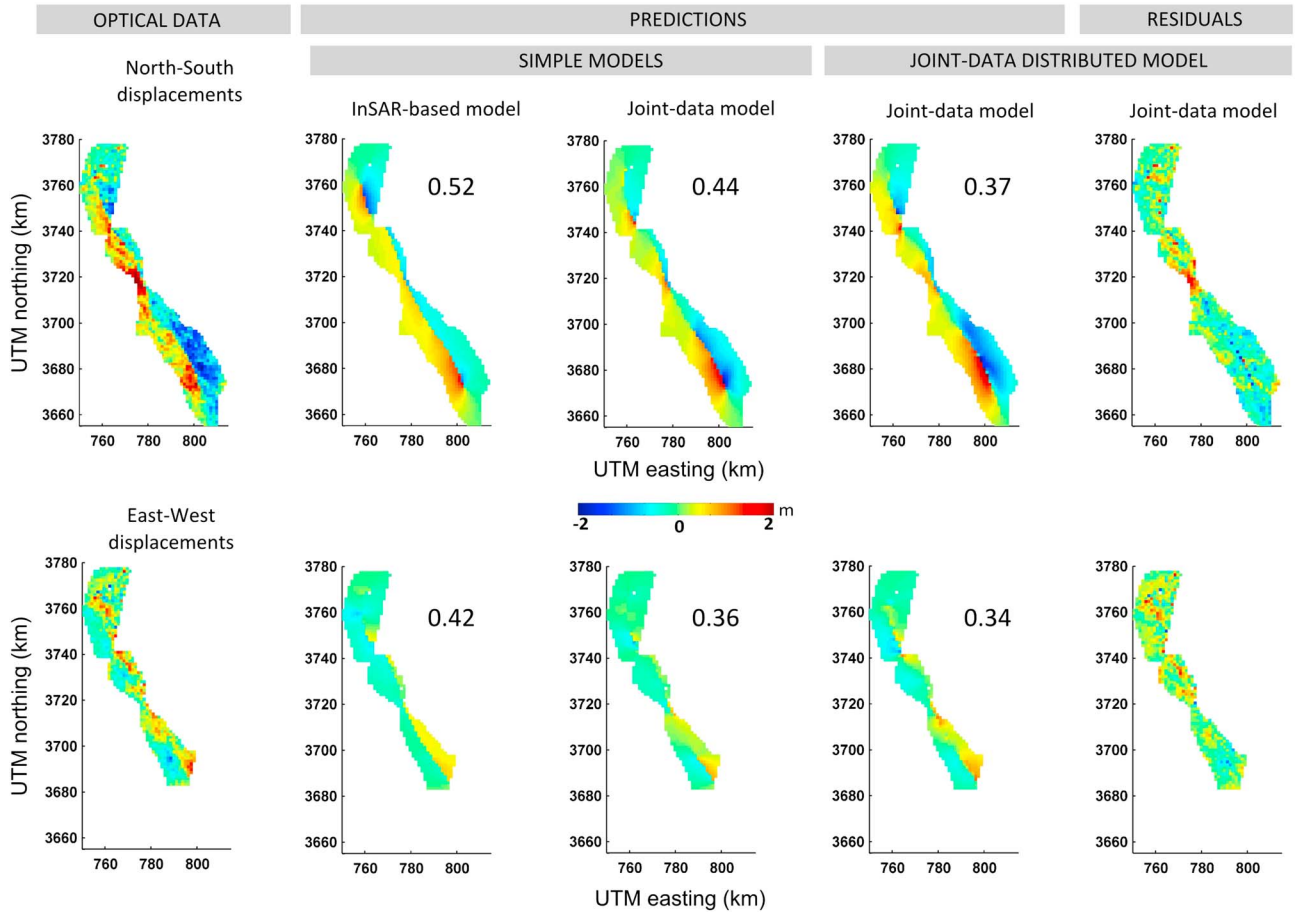

Figure 6. Optical data and model predictions. The first column represents the optical data (NS displacements for C1, C2, and C3 at the top and EW displacement of C1 and C2 at the bottom). The second and the third columns represent the predictions of the uniform slip InSAR-based and of the uniform slip joint-data models, respectively. The fourth and fifth columns represent the predictions and residuals of the joint-data distributed slip model, respectively. For each model, the RMS value is shown in meters.

As in the InSAR-based optimization, the southernmost segments (14–15) have a significant reverse component with a rake of 150°.

To summarize, both models have an average slip of 1.3 m and a moment magnitude of 7.1. The fault is dipping westward in the north and eastward in the south. In the InSAR-based model, the slip is almost homogeneous along the fault and the change in fault dip is about 15° (near segment 7), whereas in the joint-data model, the slip shows more variability along the fault and the change in fault dip is larger, about 25°, and located farther south (segment 11). These differences are due to the lack of InSAR data close to the fault (see Figure 1). The static displacement field decreases very quickly with the distance to the fault (Page et al., 2009); thus, the local faulting features are not recorded by intermediate-field data. Therefore, optimizing InSAR data only gives a smoothed version of the fault geometry and slip.

In order to investigate the robustness of the joint-data model, we repeat the joint-data optimization 50 times. The results of the first-order parameter trade-off analysis are shown in Figures S6 and S7, and the mean value of each parameter and their associated standard deviations are plotted in Figure S8 (supporting information). The model parameters of segments that exhibit high slip are not or only very slightly correlated (segments 4, 5, 13, 14, and 15) except for segment 10 which shows a clear linear dependance between the parameters. In this area, the optical surface data cover only a very narrow area on both sides of the fault which may explain a large range of parameters fitting the data equally well. However, all tests favor a west dipping segment. Concerning the low slip segments (segments 7, 8, 11, 12, and 16), only the dip-slip and strike-slip components are well constrained by the surface displacement data but not the fault dip. Indeed, if a segment does not slip, surface data cannot constrain the dip of the segment. Thanks to the dip penalty function (see section 4.2.3),

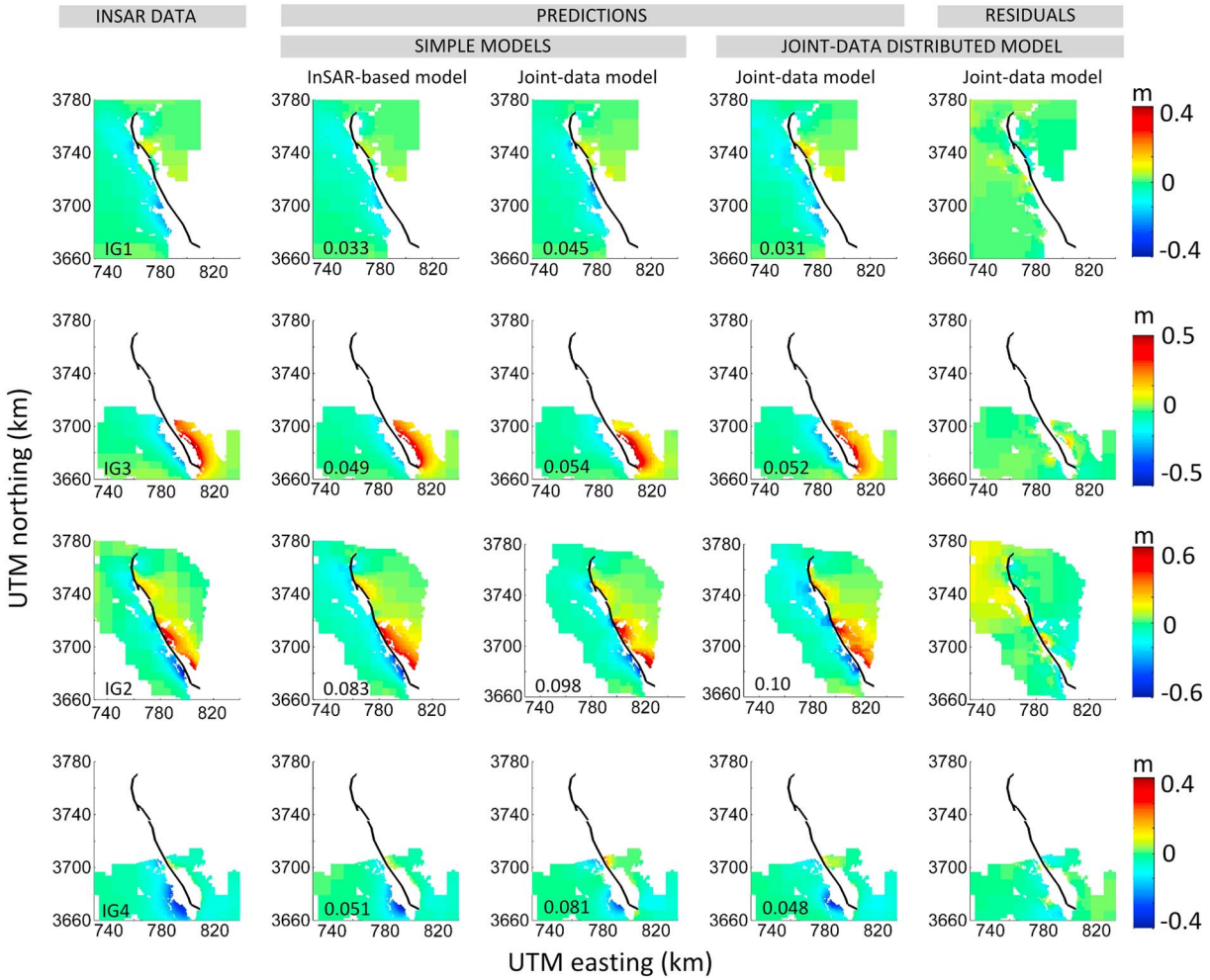

Figure 7. InSAR data and model predictions. The first column represents the InSAR data. The second and the third columns represent the predictions of the uniform slip InSAR-based and of the uniform slip joint-data models, respectively. The fourth and fifth columns represent the predictions and residuals of the joint-data distributed slip model, respectively. For each model, the RMS value is shown in meters. The black lines represent the modeled fault segments.

the high slip and well-constrained segments transmit their dip to the neighboring low slip and less constrained segments. This analysis suggests that the change of dip near the center part of the fault is a reliable feature of the Abiz fault, although its sharpness could be overestimated. Furthermore, the robustly estimated very low slip on segment 16 suggests that this segment has not been activated during the earthquake, even though it was mapped in the field by Berberian et al. (1999).

5.2. Distributed Slip Model Results

As in the previous section, we run two inversions to obtain both the InSAR-based distributed slip model and the joint-data distributed slip model using the geometries obtained in the genetic algorithm optimizations. The data sets used in the joint-data inversion are the InSAR and optical displacement fields and the optical offsets across the fault (section 4.3.1). We remove segment 16 from the inversion because none of the uniform slip models indicate slip on this segment and we extend the length of segment 15 at its southern end. Also, in this joint-data inversion, we do not apply any smoothing between segments 10 and 11 where the fault dip changes sharply (Figure 8).

For the InSAR-based model, model predictions of InSAR data are very good with a mean RMS misfit of 0.04 m whereas the model still fails to predict the principal features of the optical data (see Figures S9 and S10 in the supporting information). The joint-data model predictions are in good agreement with both InSAR and optical data (Figures 6 and 7). The RMS misfit to the NS optical-correlation displacements decreases from 0.44 m in the uniform-slip segment model to 0.37 m in the distributed slip model. The improvement of the model fit is particularly visible in the south on the western side of the fault, and also in the central part of the fault.

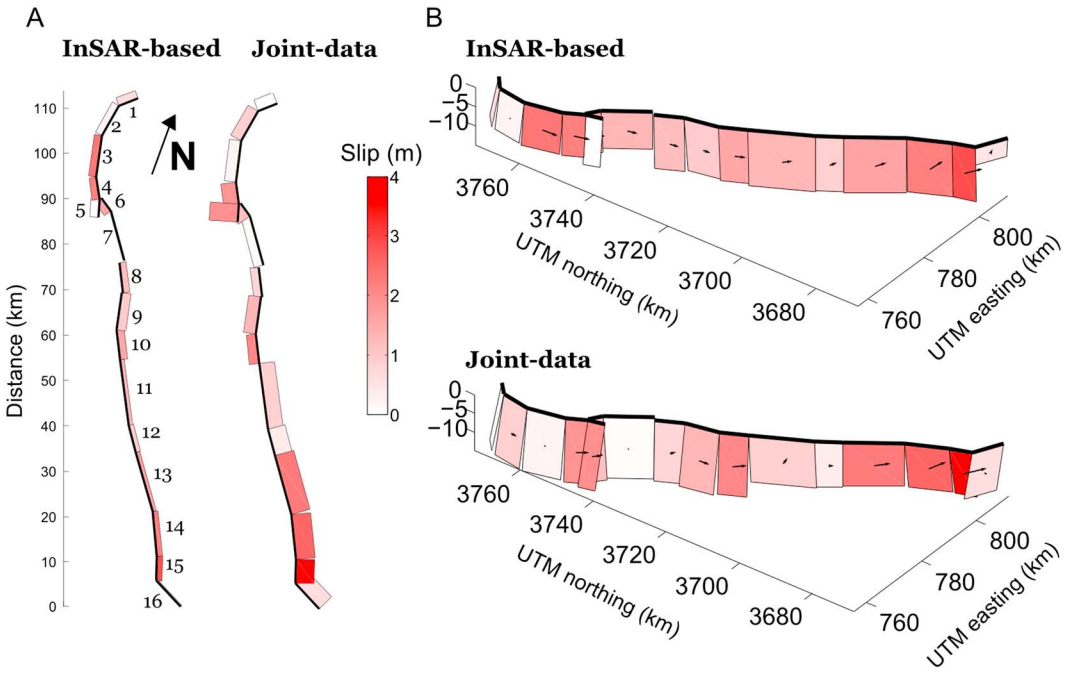

Figure 8. Uniform slip models obtained from the genetic algorithm by inverting InSAR data alone (InSAR-based model) or by inverting jointly InSAR and optical data (Joint-data model). The models are represented (a) in top view and (b) in side view. The color represents the slip amplitude on each segment, while the arrows represent movement of the eastern block with respect to the western block.

The joint-data model also predicts the offsets across the fault well (see Figure S11 in the supporting information), with an RMS between data and predictions of about 0.40 m.

Concerning the slip distribution on the fault plane, both distributed slip models show three major slip patches (Figure 9). However, the slip amplitude and the shape of these patches are different between the two models. In the joint-data model, the amplitude of the slip within each patch is systematically higher (maximum about 4.5 m) than in the InSAR-based model (maximum about 3 m). The three slip patches of the joint-data model are separated by zones of very low slip, whereas they are more connected in the InSAR-based model (see isoline 1 m). In the joint-data model, the three patches have a larger along strike extent than in the InSAR-based model (30 km versus 20 km in the north, 20 km versus 10 km in the center, and 40 km versus 20 km in the south). Finally, the three patches are not strictly located at the same place on the fault plane. In the joint-data model, the northern slip patch is more centered on the epicenter of the earthquake and thus located deeper. The central slip patch is located farther north (segments 8 to 10) in the joint-data model than in the InSAR-based model (segments 10 and 11). All these differences make the joint-data model rougher than the InSAR-based model, with more concentrated slip in localized zones on the fault plane. Both models present an important dip-slip component on the southernmost segments (segments 14 and 15). Interestingly, in the joint-data model, the southern end of each slip patch shows an important dip-slip component; downward for the northern and central patches (see segments 6, 10 and 11) and upward for the southern patches (segment 15). The geodetic moment is 1×10^{20} Nm and 8×10^{19} Nm for the joint-data model and the InSAR-based model, respectively, which leads to a higher moment magnitude for the joint-data model (7.3 versus 7.2, assuming a rigidity of 3×10^{10} Nm^{-2}). The resulting pseudo-focal mechanisms of both models are consistent and lead to a predominantly strike-slip focal mechanism with a small reverse component as inferred from the seismological data (Figures 1 and 9, Berberian et a., 1999).

In order to investigate the effect of the fault geometry uncertainty on the slip distribution, we run the joint inversion 50 times using the 50 different fault geometries obtained with the genetic algorithm (section 5.1). We define the slip uncertainty on each subfault as the standard deviation of the subfault slip obtained from the 50 inversions. The results are presented in Figure S13 (supporting information). They show that the mean standard deviation is the lowest in the southern part of the fault (0.08 m, segments 11–15) and the largest in the central part (0.27 m, segments 4–10). Slip uncertainties are highest where dip uncertainties

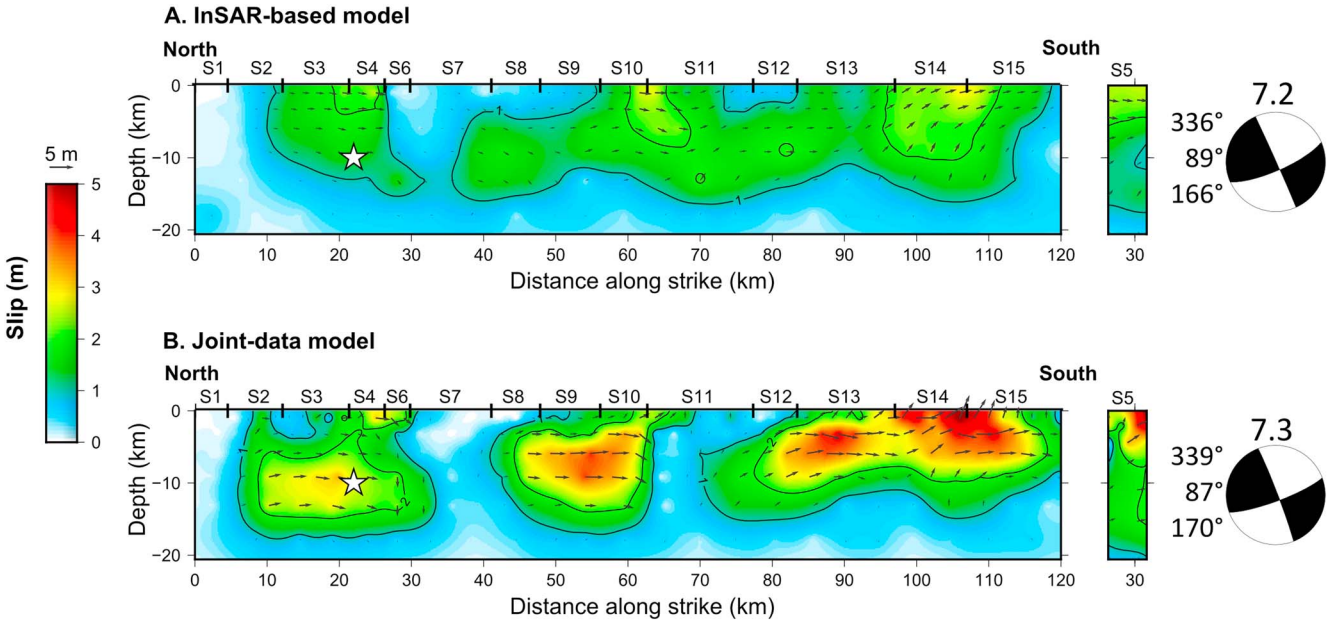

Figure 9. Interpolated distributed slip model constrained by InSAR data only (a) and by both InSAR and optical data (b). The interpolated color represents the slip amplitude whereas the black arrows represent the slip direction of the eastern side of the fault with respect to the western side. The white star indicates the epicenter and the thin black lines are the 1 m and 2 m isolines. Segment 5 is displaced for visibility; see Figure 4 for its original location. The noninterpolated views of the slip models are available in Figure S12 of the supporting information. Pseudo-fault mechanisms calculated from the fault models are plotted to the left of each model. The numbers next to them give the strike, dip, and rake values, from top to bottom, respectively. The moment magnitude is plotted above each pseudo-focal mechanism.

are largest (Figures S8 and S13). Even though slip uncertainties vary along the fault, the mean slip standard deviation is quite low with respect to the slip amplitude. The amplitude and pattern of the slip distribution are thus quite robust.

6. Discussion

6.1. InSAR-Based Model Versus Joint-Data Model

Results presented in the previous section show that the addition of near-field optical data in the modeling changes the obtained fault geometry, the slip amplitude, and the slip distribution at depth significantly.

Concerning the fault geometry, no significant difference is highlighted in the northern section of the fault in the case of either including or excluding optical data (segments 1–6). As shown in the trade-off parameter analysis, the dip is not as well constrained in the central section of the fault (segments 7–10) than in the southern section (segments 11–16). In the central section, the difference in dip between the InSAR-based and joint-data uniform models could thus mostly reflect the parameter uncertainties but not in the southern section. The optical near-field data should be sensitive to the dip in the uppermost few kilometers, whereas the InSAR intermediate-field data should be sensitive to dip at greater depths. Our results could thus suggest an increase of dip with depth. Finally, the stability analysis indicates a 15° to 30° dip variation between segments 10 and 11. Such a strong dip change along strike has already been modeled for other large strike-slip earthquakes such as the 2010 Mw7.2 El Mayor Cucapah earthquake (Wei et al., 2011). Moreover, the direction of the dip along the fault and the location of the dip change is in agreement with the coseismic vertical movements observed by Berberian et al. (1999) in the field. They observed uplift of the west block in the north and of the east block in the south with the change occurring in the northern part of segment 11.

A straightforward explanation for the slip amplitude difference between the InSAR-based model and the joint-data model (Figure 9) is the spatial data coverage. However, other causes can be discussed.

First, all our data sets span long and different durations of postseismic period and therefore could include different proportions of measurable postseismic deformation (see, e.g., Freed, 2005; Wright et al., 2013, for reviews). The InSAR data set covers between 2 months and 2 years of the postseismic period and the optical

data set between 3 and 8 years. The very small residuals of the InSAR-based distributed slip model suggest that the four interferograms are consistent with each other (Figure S9). It follows that the contribution of the postseismic deformation toward the InSAR signal in the first 2 years after the earthquake is insignificant compared to the contribution of the coseismic plus postseismic deformation in the first 2 months. The same holds for surface displacements in the even longer postseismic period included in the optical data set (3 to 8 years). Moreover, at this time scale, it is assumed that the remaining process is one that affects the volume surrounding the fault and should not affect the very near-field displacements (e.g., Hearn et al., 2009). Consequently, we think the difference in postseismic coverage between the InSAR and optical data sets cannot explain the difference in slip amplitude between the fault models.

Second, a part of the slip amplitude difference between the models can be explained by the fact that we made the hypothesis of a homogeneous elastic medium (Okada, 1992). Indeed, in the shallow part of the crust, the materials are weaker, so less slip is needed to produce surface displacements. Modeling the fault slip in a homogeneous medium may overestimate the slip to fit the near-field data. Modeling the fault slip in a layered medium could reconcile both slip distribution models, but no specific geophysical data are available to infer a realistic 1-D layered model in the area.

Third, the strength of the smoothing also affect the slip amplitude. Indeed, when increasing the smoothing factor, the fit to near-field optical data (within 10 km of the fault) deteriorates faster than the fit to intermediate-field InSAR data. Hence, the InSAR-based model is smoother than the joint-data model and consequently the slip amplitude is lower.

Finally, the location of the three slip zones is slightly different between both models of the slip distribution. This suggests that near-field data are necessary to precisely locate the contour of the slip zones.

6.2. Rupture Propagation Controlled by the Fault Geometry

Our best model shows three slip patches (Figures 8 and 9b) located directly above the zones of localized and high surface displacements, as highlighted in the optical displacement maps (section 3.2 and Figure 2). Low slip zones separate those three patches and correspond to distributed displacement zones at the surface. Moreover, we can relate these low slip areas to geometrical complexities of the Abiz fault. Indeed, the northern low slip zone corresponds to the end of the curved part of the Abiz fault and to a change of the fault strike (segment 7), and the second zone to a sharp dip change (segment 10, Figure 8). These geometric complexities have also been mapped in the field. The southern one is described by Berberian et al. (1999) as an en-echelon step over of at least 800 m wide, is characterized by a broad zone of distributed shear, and corresponds to the transition between the relatively flat topography of the Zirkuh plain in the north and the mountain range in the south.

The dip-slip component modeled at the southern end of each main slip patch is also in agreement with Berberian et al. (1999) who measured 70 cm of dip-slip near 3,740 km northing, and 90 cm near 3,675 km northing. Moreover, these reverse components of slip are also supported by seismological data (see subevent moment tensors 2 and 4 of Berberian et al., 1999, in Figure 1b). A similar transition from strike-slip to dip-slip at the end of the slip patches has already been described for the Kokoxili earthquake (Mw 7.8, 2001) and was interpreted as the transition between slipping segments and geometric barriers (Klinger et al., 2006).

About 5 days after the earthquake, two temporary independent seismological networks were deployed for a period of 2 months in order to record the aftershock activity. Farahbod et al. (2003) analyzed the data of aftershocks recorded by both networks and relocated them. They obtained a catalog of 215 relocated events, plotted in Figure 10. For most of these events, the hypocenter uncertainty is less than or equal to 5 km.

The relocated aftershocks are not localized on the fault plane but are spread over a larger area on both sides of the fault. At both ends of the rupture few aftershocks have occurred. At the northern end, it can be explained by the unilateral southward propagation of the rupture. At the southern end, however, the fault slip is maximal and stops abruptly (segment 15). A large cluster of aftershocks is located where the fault dip reverses (segment 10), and a smaller cluster of aftershocks is located farther north, where the strike changes significantly (segment 7). These two clusters are both located at the edges of high slip patches. Anticorrelation between aftershock locations and areas of large coseismic slip has been observed for other earthquakes (e.g., Cirella et al., 2009; Sladen et al., 2010; Tong et al., 2010; Wei et al., 2011) and is often explained by stress release in areas loaded by the coseismic deformation (Das & Henry, 2003; Mendoza & Hartzell, 1988).

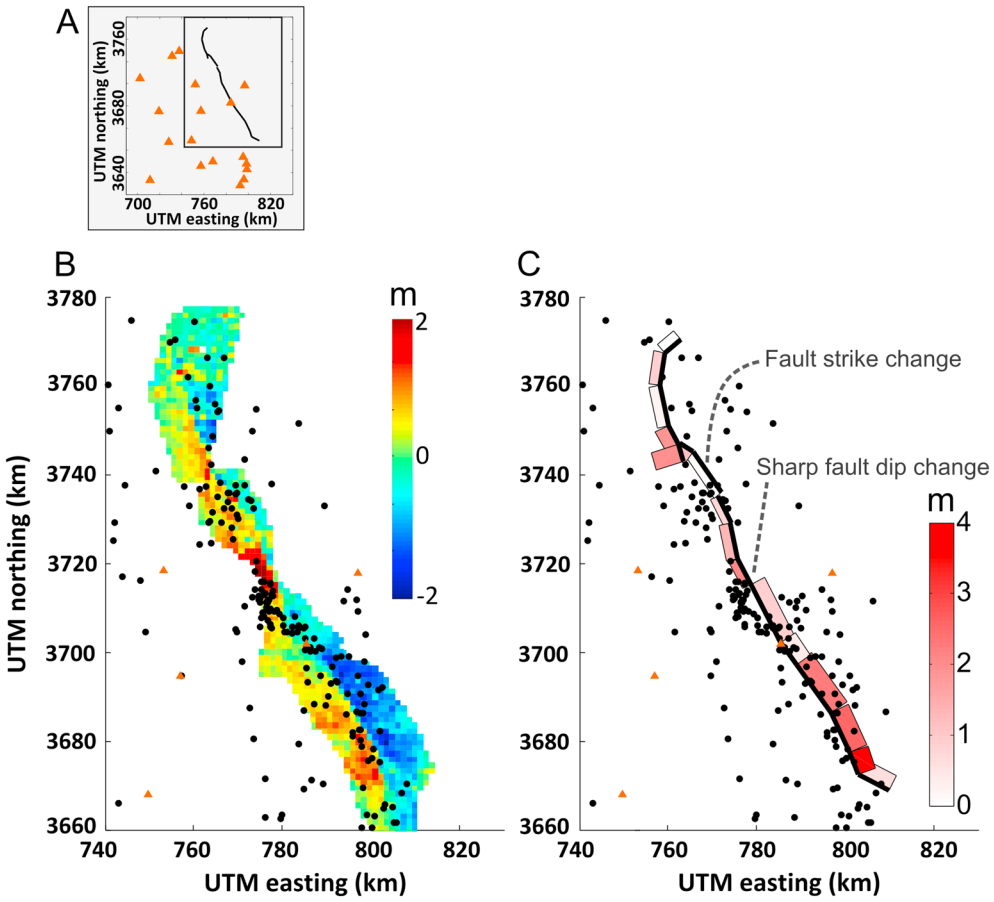

Figure 10. Overview of near-fault NS surface displacements, fault geometry, fault slip, and aftershocks. (a) Location of the temporal seismic network deployed after the mainshock. The orange triangles are the seismic stations, the black line represents the Abiz fault, and the black rectangle is the location of Figures 10b and 10c. (b) NS optical-correlation surface displacement. (c) Uniform-slip segment joint-data model. In (b) and (c), black dots show the aftershock recorded from 15 days to 2.5 months after the earthquake (Farahbod et al., 2003) and the five orange triangles are the near-fault seismic stations.

It is thus clear from the surface displacement data, the fault model, and the aftershock distribution that the Abiz fault can be divided into three main segments: (1) The northern segment is about 35 km long (segments 1–6) and is characterized by the pronounced curvature of the Abiz fault. (2) The central segment is 34 km long (segments 7–10) and ends where the fault dip reverses. (3) The southern segment is 50 km long and extends from the dip change to the southern end of the Abiz fault (segments 11–15).

Interestingly, the northern and central segments are mapped as consisting of at least four segments each by Berberian et al. (1999), whereas the longest segment in the south is described as consisting of two segments only. The longest slipping segment thus seems to be structurally most simple. Geometric complexities, such as fault bends and step overs, are known to impede or obstruct the rupture propagation of earthquakes (e.g., King & Nabelek, 1985; Wesnousky, 2006) and are often defined as geometric barriers (Aki, 1979; Klinger et al., 2006). Similarly, the Abiz fault geometry seems to have played a major role in the rupture propagation during the 1997 Zirkuh earthquake. Indeed, we showed that the Abiz fault is composed of three main segments acting as asperities which are separated by geometrical barriers that impede the rupture propagation and where the aftershock activity locates.

6.3. Data Dependency of the Shallow Slip Deficit Estimation

For several large strike-slip earthquakes, their modeled coseismic slip showed a slip maximum located generally between ~4 km and 8 km and decreasing both toward the surface and with depth (Fialko et al., 2005). It turns out that the uppermost part of the crust (i.e., between 0 km and 4 km) exhibits a coseismic shallow slip deficit (SSD). This observation raises questions about (1) the mechanisms that prevent the fault slip

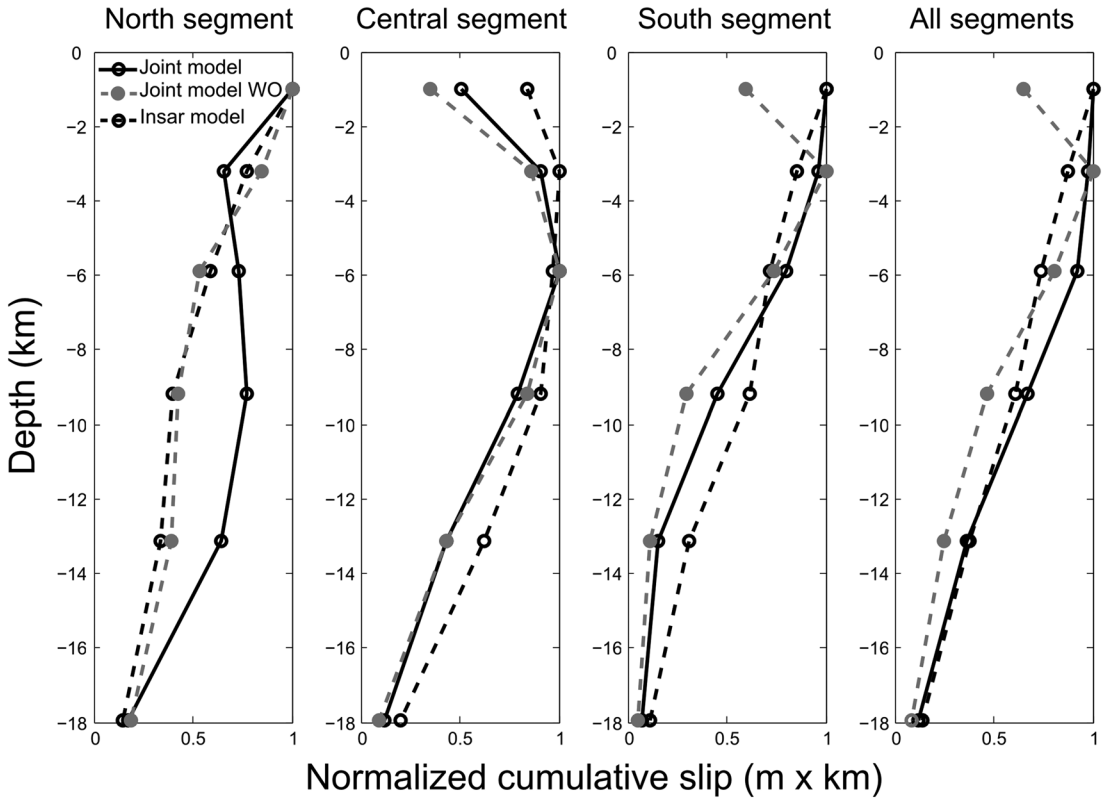

Figure 11. Normalized cumulative slip as a function of depth for the northern, central, southern, and all three segments of the Abiz fault. The black line represents the joint-data model with the offsets included in the inversion, the gray dotted line represents the joint-data model without the offsets (WO joint-data model), and the black dotted line represents the InSAR-based model.

from propagating fully up to the surface, (2) the processes that accommodate this SSD through the earthquake cycle or over several earthquake cycles, and last but not least, (3) our ability to evaluate accurately the seismic hazard that is often based on slip rates deduced from surface offsets measured in the field. SSD was discussed in numerous studies that aim to explain the processes that favor it or how it is accommodated through the earthquake cycles (e.g., Dolan & Haravitch, 2014; Fialko et al., 2005; Tong et al., 2010).

Recently, Xu et al. (2016) claimed that most of the apparent SSD based on geodetic inversions is an artifact due to the lack of data coverage close to the surface rupture. They tested their assumption in reassessing the fault slip model of three large strike-slip earthquakes using near-field observations, mostly from optical correlation offsets, in addition to InSAR and GPS surface displacement observations. In their new fault slip models, the apparent SSD decreases drastically (between 3% and 19% versus 20% and 60% in previous studies). Fault slip models of the recent 2013 Balochistan strike-slip earthquake (Mw 7.7), based on multidata sets among which include optical-correlation displacement data, show some quite homogeneous slip distribution with depth and thus little SSD (Avouac et al., 2014; Jolivet et al., 2014).

Here we estimate the SSD for the three distributed fault slip models we obtained: (1) the InSAR-based model, (2) the joint-data model without the offsets and pixels located on the fault (WO joint-data model), and (3) the full joint-data model (see section 5.2). For each model, we calculate the SSD for the entire Abiz fault and for each of the three segments highlighted by our inversion (Figure 11). We integrate the slip along the fault trace as a function of depth and then normalize the cumulative slip at each depth by the maximum cumulative slip (Xu et al., 2016). Whatever the model, the slip is rather concentrated in the upper 10 km of the crust, except in the northern section where the joint-data model slip concentrates both at the surface and at the epicentral depth. The SSD for the entire fault is null for the joint-data and InSAR-based models, whereas it is about 35% in the WO joint-data model. None of the models display SSD on the northern segment, and all models display SSD on the central segment, with 75% of SSD in the WO joint-data model, 50% of SSD in the joint-data model, and 20% in the InSAR-based model. On the southern segment, the WO joint-data model has 40% of SSD, whereas the other slip models do not show a SSD.

Contrary to the conclusion of Xu et al. (2016), our InSAR-based model, which does not incorporate near-field observations, displays the smallest SSD. However, although both joint-data models predict larger SSD, the inclusion of optical offsets in the inversion leads to a drastic decrease of the SSD. The WO SSD joint-data model could be explained by off-fault deformation occurring at shallow depths during the earthquake (Kaneko & Fialko, 2011; Milliner et al., 2015; Zinke et al., 2014). Indeed, when we model the fault with a unique fault plane, the off-fault deformation will be interpreted in the inversion as slip occurring at depth (Simons et al., 2002). The shallow slip will then be underestimated and the deeper slip overestimated. The optical offsets, measured across the fault, encompass the off-fault deformation (or at least a part of it). Consequently, including the optical offsets in the inversion will result in a smaller SSD. The SSD obtained for an earthquake is thus very dependent on the data used.

The SSD on the central segment seems to be a robust feature as it is present in all models. An explanation could be that the off-fault deformation in the central segment occurred over a larger width than in the northern and southern segments. Consequently, all the off-fault deformation would not be included in the optical offset estimations. The discrepancy between the SSD of the InSAR-based and the joint-data models on the central segment could be due to the difference in the smoothing applied. Indeed, the increase of the smoothing factor reduces the SSD (Xu et al., 2016) and as stated in section 6.1 the InSAR-based model is smoother than the joint-data model.

A variation of off-fault deformation width between the central segment and the other segments could be explained by an along-strike difference in the type of near-surface materials, as several studies have shown (e.g., Milliner et al., 2015; Teran et al., 2015). The regional geological maps at 1/250,000 (Geological Survey and Mineral Exploration of Iran, 1982) show that the central segment is surrounded by unconsolidated Quaternary material, whereas the northern segment traverses basement rocks on the western side and Quaternary deposits on the eastern side and the southern segment traverses basement rocks. This observation is consistent with studies that show that a sediment/sediment interface promotes off-fault deformation, whereas a basement/basement or basement/sediment interface does not (Treiman et al., 2002; Zinke et al., 2014). To conclude, we found that except for the central segment, the Zirkuh earthquake does not show a SSD, as expected for a mature fault like the Abiz fault (Dolan & Haravitch, 2014); the SSD found in the central segment could be due to off-fault deformation in unconsolidated Quaternary deposits.

7. Conclusion

We infer an updated fault slip model for the Zirkuh earthquake using near-field displacement data from optical image correlation and intermediate-field displacement data from InSAR. This study illustrates the importance of near-field data in refining the geometry of the fault and imaging the slip distribution on the fault plane more precisely. In particular, we show that a clear change of fault dip between the central and southern segments is required to fit the optical-correlation displacement data. Moreover, we find that the use of near-field data lead to an increased slip amplitude and an increased slip distribution roughness. The modeled slip distribution confirms that the Zirkuh earthquake ruptured three main asperities on the Abiz fault that are separated by geometric barriers: high slip patterns are found where the fault geometry is rather smooth, whereas low slip, associated with a thrust component, is found where the fault geometry is more complex. These geometric complexities and areas of low slip match the location of clusters of aftershocks recorded after the main shock. Finally, at the fault scale, this Mw 7.2 strike-slip earthquake does not exhibit an overall shallow slip deficit. However, locally, we find a shallow slip deficit along the central segment that could be explained by off-fault deformation in unconsolidated Quaternary deposits.

Acknowledgments
The study was supported by the Agence Nationale de la Recherche (ANR, French National Research Agency) through the "E-POST" project under the contract ANR-14-CE03-0002. The SPOT images are Astrium products and have been purchased via the ISIS French program. ASTER GDEM is a product of METI and NASA and was obtained through the Reverb ECHO website. All optical images were processed using COSI-Corr (Leprince et al., 2007), which is a plug-in for the ENVI software package. We thank Amir Farahbod for providing the Zirkuh aftershock data. Several figures were created with the Generic Mapping Tools (GMT) software (Wessel et al., 2013). The surface displacement fields used in this study as well as the source code for the genetic algorithm are available in the repository Zenodo (DOI 10.5281/zenodo.1064052). We are grateful to the Editor and the two anonymous reviewers for their constructive and thorough comments that greatly helped us improve our manuscript. We are also grateful to Guust Nolet and Louisa Tsang for providing numerous grammatical and syntax improvements.

References

Adams, M., Twardzik, C., & Ji, C. (2017). Exploring the uncertainty range of coseismic stress drop estimations of large earthquakes using finite fault inversions. *Geophysical Journal International*, *208*, 86–100. https://doi.org/10.1093/gji/ggw374

Aki, K. (1979). Characterization of barriers on an earthquake fault. *Journal of Geophysical Research*, *84*(9), 6140–6148.

Atzori, S., Tolomei, C., Antonioli, A., Boncori, J. P. M., Bannister, S., Trasatti, E., … Salvi, S. (2012). The 2010–2011 Canterbury, New Zealand, seismic sequence: Multiple source analysis from InSAR data and modeling. *Journal of Geophysical Research*, *117*, B08305. https://doi.org/10.1029/2012JB009178

Avouac, J.-P., Ayoub, F., Wei, S., Ampuero, J.-P., Meng, L., Leprince, S., … Helmberger, D. (2014). The 2013, Mw 7.7 Balochistan earthquake, energetic strike-slip reactivation of a thrust fault. *Earth and Planetary Science Letters*, *391*, 128–134. https://doi.org/10.1016/j.epsl.2014.01.036

Ayoub, F., Leprince, S., & Avouac, J.-P. (2009). ISPRS Journal of Photogrammetry and Remote Sensing Co-registration and correlation of aerial photographs for ground deformation measurements. *ISPRS Journal of Photogrammetry and Remote Sensing*, *64*(6), 551–560. https://doi.org/10.1016/j.isprsjprs.2009.03.005

Ayoub, F., Leprince, S., & Avouac, J.-P. (2015). *User's guide to COSI-CORR co-registration of optically sensed images and correlation* (p. 1–49). Pasadena, CA: California Institute of Technology.

Barnhart, W. D., & Lohman, R. B. (2010). Automated fault model discretization for inversions for coseismic slip distributions. *Journal of Geophysical Research*, *115*, B10419. https://doi.org/10.1029/2010JB007545

Berberian, M., Jackson, J. A., Qorashi, M., Khatib, M. M., Priestley, K., & Talebian, M. (1999). The 1997 May 10 Zirkuh (Qa'enat) earthquake (Mw 7.2): Faulting along the Sistan suture zone of eastern Iran. *Geophysical Journal International*, *136*, 671–694.

Berberian, M., & Yeats, R. S. (1999). Patterns of historical earthquake rupture in the Iranian Plateau. *Bulletin of Seismological Society of America*, *89*, 120–139. https://doi.org/10.1016/B978-0-444-63292-0.00016-8

Beyer, H.-G., & Schwefel, H.-P. (2002). Evolution strategies: A comprehensive introduction. *Natural Computing*, *1*(1), 3–52.

Buades, A., Coll, B., & Morel, J.-M. (2008). Nonlocal image and movie denoising. *International Journal of Computer Vision*, *76*, 123–139. https://doi.org/10.1007/s11263-007-0052-1

Chilés, J.-P., & Delfiner, P. (1999). *Geostatistics: Modelling spatial uncertainties, Wiley Series in Probability and Statistics. Applied Probability and Statistics Section*. New York: John Wiley.

Cirella, A., Piatanesi, A., Cocco, M., Tinti, E., Scognamiglio, L., Michelini, A., … Boschi, E. (2009). Rupture history of the 2009 L' Aquila (Italy) earthquake from non-linear joint inversion of strong motion and GPS data. *Geophysical Research Letters*, *36*, L19304. https://doi.org/10.1029/2009GL039795

Coleman, T. F., & Li, Y. (1992). A reflective Newton method for minimizing a quadratic function subject to bounds on some of the variables. *Journal on Optimization*, *6*(4), 1–37.

Das, S., & Henry, C. (2003). Spatial relation between main earthquake slip and its aftershock distribution. *Reviews of Geophysics*, *41*(3), 1013. https://doi.org/10.1029/2002RG000119

Delouis, B., Giardini, D., Lundgren, P., & Salichon, J. (2002). Joint inversion of InSAR, GPS, teleseismic, and strong-motion data for the spatial and temporal distribution of earthquake slip: Application to the 1999 Izmit mainshock. *Bulletin of Seismological Society of America*, *92*, 278–299.

Dolan, J. F., & Haravitch, B. D. (2014). How well do surface slip measurements track slip at depth in large strike-slip earthquakes? The importance of fault structural maturity in controlling on-fault slip versus off-fault surface deformation. *Earth and Planetary Science Letters*, *388*, 38–47. https://doi.org/10.1016/j.epsl.2013.11.043

Engdahl, E. R., Jackson, J. A., Myers, S. C., Bergman, E. A., & Priestley, K. (2006). Relocation and assessment of seismicity in the Iran region. *Geophysical Journal International*, 761–778. https://doi.org/10.1111/j. 1365-246X.2006.03127.x

Farahbod, A., Lindholm, C., Mokhtari, M., & Bungum, H. (2003). Aftershock analysis for the 1997 Ghaen-Birjand (Ardekul) earthquake. *Journal of Seismology and Earthquale Engineering*, *5*(2), 1–10.

Fialko, Y., Sandwell, D., Simons, M., & Rosen, P. (2005). Three-dimensional deformation caused by the Bam, Iran, earthquake and the origin of shallow slip deficit. *Nature*, *435*, 295–299. https://doi.org/10.1038/nature03425

Freed, A. M. (2005). Earthquake triggering by static, dynamic, and postseismic stress transfer. *Annual Review of Earth and Planetary Sciences*, *33*, 335–367. https://doi.org/10.1146/annurev.earth.33.092203.122505

Funning, G. J., Parsons, B., & Wright, T. J. (2007). Fault slip in the 1997 Manyi, Tibet earthquake from linear elastic modelling of InSAR displacements. *Geophysical Journal International*, *169*(3), 988–1008. https://doi.org/10.1111/j.1365-246X.2006.03318.x

Geological Survey and Mineral Exploration of Iran (1982). Geological quadrangle maps of Iran No I.7, K.7, and I.8.Retrieved from http://www.gsi.ir/en/Maps/Maps.html

Gombert, B., Duputel, Z., Jolivet, R., Doubre, C., Rivera, L., & Simons, M. (2017). Revisiting the 1992 Landers earthquake: A Bayesian exploration of co-seismic slip and off-fault damage. *Geophysical Journal International*, *212*, 839–852. https://doi.org/10.1093/gji/ggx455

Hainzl, S., Enescu, B., Cocco, M., Woessner, J., Catalli, F., Wang, R., & Roth, F. (2009). Aftershock modeling based on uncertain stress calculations. *Journal of Geophysical Research*, *114*, B05309. https://doi.org/10.1029/2008JB006011

Hamling, I. J., Hreinsdóttir, S., Clark, K., Elliott, J., Liang, C., Fielding, E., … Stirling, M. (2017). Complex multi-fault rupture during the 2016 Mw 7.8 Kaikoura earthquake, New Zealand. *Science*, *356*, 6334. https://doi.org/10.1126/science.aam7194.promoting

Hanssen, R. (2001). Radar interferometry, data interpretation and error analysis, *Remote Sensing and Digital Image Processing* (Vol. 2, 328 pp.). Dordrecht: Kluwer Academic Publishing.

Hearn, E. H., Mcclusky, S., Ergintav, S., & Reilinger, R. E. (2009). Izmit earthquake postseismic deformation and dynamics of the North Anatolian Fault Zone. *Journal of Geophysical Research*, *114*, B08405. https://doi.org/10.1029/2008JB006026

Jolivet, R., Duputel, Z., Riel, B., Simons, M., Rivera, L., Minson, S. E., … Fielding, E. J. (2014). Short Note The 2013 Mw 7.7 Balochistan earthquake: Seismic potential of an accretionary wedge. *Bulletin of Seismological Society of America*, *104*(2), 1020–1030. https://doi.org/10.1785/0120130313

Jonsson, S., Zebker, H., Segall, P., & Amelung, F. (2002). Fault slip distribution of the 1999 Mw 7.1 Hector Mine, California, earthquake, estimated from satellite radar and GPS measurements. *Bulletin of Seismological Society of America*, *92*(4), 1377–1389.

Kaneko, Y., & Fialko, Y. (2011). Rupture simulations with elasto-plastic off-fault response. *Geophysical Journal International*, *186*, 1389–1403. https://doi.org/10.1111/j.1365-246X.2011.05117.x

King, G., & Nabelek, J. (1985). Role of fault bends in the initiation and termination of earthquake rupture. *Science*, *228*, 984–987.

Klinger, Y., Michel, R., & King, G. C. P. (2006). Evidence for an earthquake barrier model from Mw 7.8 Kokoxili (Tibet) earthquake slip-distribution. *Earth and Planetary Science Letters*, *242*(3–4), 354–364. https://doi.org/10.1016/j.epsl.2005.12.003

Konca, A. O., Leprince, S., Avouac, J.-P., & Helmberger, D. V. (2010). Rupture process of the 1999 Mw 7.1 Duzce earthquake from joint analysis of SPOT, GPS, InSAR, strong-motion, and teleseismic data: A supershear rupture with variable rupture velocity. *Bulletin of Seismological Society of America*, *100*(1), 267–288. https://doi.org/10.1785/0120090072

Lasserre, C., Peltzer, G., Crampe, F., Klinger, Y., & Woerd, J. V. D. (2005). Coseismic deformation of the 2001 $M_w = 7.8$ Kokoxili earthquake in Tibet, measured by synthetic aperture radar interferometry. *Journal of Geophysical Research*, *110*, B12408. https://doi.org/10.1029/2004JB003500

Leprince, S., Barbot, S., Ayoub, F., & Avouac, J.-P. (2007). Automatic and precise orthorectification, coregistration, and subpixel correlation of satellite images, application to ground deformation measurements. *IEEE Transactions on Geoscience and Remote Sensing*, *45*(6), 1529–1558.

Massonnet, D., Rossi, M., Carmona, C., Adragna, F., Peltzer, G., Feigl, K., & Rabaute, T. (1993). The displacement field of the Landers earthquake mapped by radar interferometry. *Nature*, *364*, 138–142.

Mendoza, C., & Hartzell, S. H. (1988). Aftershock patterns and main shock faulting. *Bulletin of the Seismological Society of America*, *78*(4), 1438–1449.

Michel, R., & Avouac, J.-P. (2002). Deformation due to the 17 August 1999 Izmit, Turkey, earthquake measured from SPOT images. *Journal of Geophysical Research*, *107*(B4), 2062. https://doi.org/10.1029/2000JB000102

Milliner, C. W. D., Dolan, J. F., Hollingsworth, J., Leprince, S., Ayoub, F., & Sammis, C. G. (2015). Quantifying near-field and off-fault deformation patterns of the 1992 Mw 7.3 Landers earthquake. *Geochemistry, Geophysics, Geosystems*, *16*, 1577–1598. https://doi.org/10.1002/2014GC005693

Monelli, D., & Mai, P. M. (2008). Bayesian inference of kinematic earthquake rupture parameters through fitting of strong motion data. *Geophysical Journal International*, *173*(1), 220–232. https://doi.org/10.1111/j.1365-246X. 2008.03733.x

Okada, Y. (1992). Internal deformation due to shear and tensite faults in a half-space. *Bulletin of Seismological Society of America*, *82*(2), 1018–1040.

Page, M. T., Custo, S., Archuleta, R. J., & Carlson, J. M. (2009). Constraining earthquake source inversions with GPS data: 1. Resolution-based removal of artifacts. *Journal of African Earth Sciences*, *114*, 1–13. https://doi.org/10.1029/2007JB005449

Parsons, T. (2004). Recalculated probability of Mw 7 earthquakes beneath the Sea of Marmara, Turkey. *Journal of Geophysical Research*, *109*, B05304. https://doi.org/10.1029/2003JB002667

Puymbroeck, V., Binet, R., & Avouac, J.-P. (2000). Measuring earthquakes from optical satellite images. *Applied Optics*, *39*(20), 3486–3494.

Reilinger, R. E., Ergintav, S., Bu, R., Mcclusky, S., Lenk, O., Barka, A., … To, M. N. (2000). Coseismic and postseismic fault slip for the 17 August 1999, earthquake. *Science*, *289*, 1519–1524.

Rosu, A.-m., Pierrot-deseilligny, M., Delorme, A., Binet, R., & Klinger, Y. (2015). ISPRS Journal of Photogrammetry and Remote Sensing Measurement of ground displacement from optical satellite image correlation using the free open-source software MicMac. *ISPRS Journal of Photogrammetry and Remote Sensing*, *100*, 48–59. https://doi.org/10.1016/j.isprsjprs.2014.03.002

Sambridge, M., & Mosegaard, K. (2002). Monte Carlo methods in geophysical inverse problems. *Reviews of Geophysics*, *40*(3), 1009. https://doi.org/10.1029/2000RG00089

Simons, M., Fialko, Y., & Rivera, L. (2002). Coseismic deformation from the 1999 Mw 7.1 Hector Mine, California, earthquake as inferred from InSAR and GPS observations. *Bulletin of Seismological Society of America*, *92*(4), 1390–1402.

Sladen, A., Tavera, H., Simons, M., Avouac, J. P., Konca, A. O., Perfettini, H., … Cavagnoud, R. (2010). Source model of the 2007 Mw 8.0 Pisco, Peru earthquake: Implications for seismogenic behavior of subduction megathrusts. *Journal of Geophysical Research*, *115*, B02405. https://doi.org/10.1029/2009JB006429

Smith, B. M. L., Scales, J. A., & Fischer, T. L. (1992). Global search and genetic algorithms. *Geophysics: The Leading Edge of Exploration*, *11*(1), 22–26.

Sudhaus, H., & Jonsson, S. (2009). Improved source modelling through combined use of InSAR and GPS under consideration of correlated data errors: Application to the June 2000 Kleifarvatn earthquake, Iceland. *Geophysical Journal International*, *176*, 389–404. https://doi.org/10.1111/j.1365-246X.2008.03989.x

Sudhaus, H., & Jonsson, S. (2011). Source model for the 1997 Zirkuh earthquake (Mw=7.2) in Iran derived from JERS and ERS InSAR observations. *Geophysical Journal International*, *185*(2), 676–692. https://doi.org/10.1111/j. 1365-246X.2011.04973.x

Teran, O. J., Fletcher, J. M., Oskin, M. E., Rockwell, T. K., Hudnut, K. W., Spelz, R. M., … Morelan, A. E. (2015). Geologic and structural controls on rupture zone fabric: A field-based study of the 2010 Mw 7.2 El Mayor-Cucapah earthquake surface rupture. *Geosphere*, *11*(3), 899–921. https://doi.org/10.1130/GES01078.1

Tong, X., Sandwell, D. T., & Fialko, Y. (2010). Coseismic slip model of the 2008 Wenchuan earthquake derived from joint inversion of interferometric synthetic aperture radar, GPS, and field data. *Journal of Geophysical Research*, *115*, B04314. https://doi.org/10.1029/2009JB006625

Treiman, J. A., Kendrick, K. J., Bryant, W. A., Rockwell, T. K., & Mcgill, S. F. (2002). Primary surface rupture associated with the Mw 7.1 16 October 1999 Hector Mine Earthquake, San Bernardino County, California. *Bulletin of Seismological Society of America*, *92*(4), 1171–1191.

Vallage, A., Klinger, Y., Grandin, R., & Bhat, H. S. (2015). Inelastic surface deformation during the 2013 Mw 7.7 Balochistan, Pakistan, earthquake. *Geology*, *43*(12), 1079–1082. https://doi.org/10.1130/G37290.1

Wei, S., Fielding, E., Leprince, S., Sladen, A., Avouac, J.-P., Helmberger, D., … Briggs, R. (2011). Superficial simplicity of the 2010 El Mayor-Cucapah earthquake of Baja California in Mexico. *Nature Geoscience*, *4*(9), 615–618. https://doi.org/10.1038/ngeo1213

Wesnousky, S. G. (2006). Predicting the endpoints of earthquake ruptures. *Nature*, *444*, 358–360. https://doi.org/10.1038/nature05275

Wessel, P., Smith, W., Scharroo, R., Luis, J., & Wobbe, F. (2013). Generic Mapping Tools: Improved version released. *Eos, Transactions American Geophysical Union*, *94*(45), 409–420.

Wright, T. J., Elliott, J., Wang, H., & Ryder, I. (2013). Earthquake cycle deformation and the Moho: Implications for the rheology of continental lithosphere. *Tectonophysics*, *609*, 504–523. https://doi.org/10.1016/j.tecto.2013.07.029

Wright, T. J., Lu, Z., & Wicks, C. (2004). Constraining the slip distribution and fault geometry of the Mw 7.9, 3 November 2002, Denali fault earthquake with interferometric synthetic aperture radar and global positioning system data. *Bulletin of Seismological Society of America*, *94*(6), 175–189.

Xu, X., Tong, X., Sandwell, D. T., Milliner, C. W. D., Dolan, J. F., Hollingsworth, J., … Ayoub, F. (2016). Refining the shallow slip deficit. *Geophysical Journal International*, *204*, 1867–1886. https://doi.org/10.1093/gji/ggv563

Zinke, R., Hollingsworth, J., & Dolan, J. F. (2014). Surface slip and off-fault deformation patterns in the 2013 M_W 7.7 Balochistan, Pakistan earthquake: Implications for controls on the distribution of near-surface coseismic slip. *Geochemistry, Geophysics, Geosystems*, *15*, 5034–5050. https://doi.org/10.1002/2014GC005538